BREAKUP DYNAMICS OF A NEUTRON-HALO SYSTEM AT SUB-BARRIER INCIDENT ENERGIES

by

Tapuwa Sithole

submitted in accordance with the requirement for

a degree of

MASTER OF SCIENCE

in the subject

PHYSICS

at the

UNIVERSITY OF SOUTH AFRICA

SUPERVISOR: PROF B. MUKERU

FEBRUARY 2024

Dedications

I dedicate this dissertation to

★ My parents Mr Billayard Mubuso Sithole and Mrs Moud Siduna Sithole

The simplicities of natural laws arise through the complexities of the language we use for expression.

EugeneWigner

Acknowledgments

Firstly, I would like to give Glory to the Lord Jesus Christ for giving me healthy life and mental strength during the period of this research. I am so grateful to him, he has shown me his compassion towards my life. Praise his name forever!

I would like to give special thanks to Professor B Mukeru for his everlasting support, love, long-suffering heart and great mentoring ability he gave me whenever I hit a bump in my research. He opened his doors whenever I came knocking. His valuable wisdom and knowledge mould the direction of love to work hard in my life.

I would like to thank my family and relatives for believing and motivating me whenever the journey was tough.

I am forever grateful to my wife Gloria Masvaure Sithole and my kids S Shannon Sithole, A Aaliyah Sithole and D Sean Sithole . Sithole family P. Rhodes, D. Edith, C. Fungai, J. Farai, S. Cames and M. Sawimbi.

Special honour and thanks to my sister Tambudzai Sithole for her prayers, love, encouragement and financial support. Thanks to everyone who contributed to my well-being and towards my completion of this degree.

Declaration

I Tapuwa Sithole declare that **"BREAKUP DYNAMICS OF A NEUTRON-HALO SYSTEM AT SUB-BARRIER INCIDENT ENERGIES"** is my own work and that all the sources that I have used or quoted have been indicated and acknowledged by means of complete references.

I further declare that I submitted the dissertation to originality checking software and that it falls within the accepted requirements of originality

I further declare that I have not previously submitted this work, or part of it, for examination at UNISA for another qualification or at any other higher education institution

——————————

Signature

Date: February 2024

Mr Tapuwa Sithole (Student Number: 36760633)

Abstract

The understanding of the nuclear breakup dynamics at sub-barrier incident energies, remains a hot subject in Nuclear Physics. In this dissertation, the breakup of the weakly-bound neutron-halo ^{11}Be nucleus impinging on a lead target is investigated for sub-barrier and around the Coulomb barrier incident energies. As theoretical framework, the continuum discretized coupled channels (CDCC) formalism is used. The fundamental mathematical description of this formalism leading to a discretized set of coupled differential equations is outlined and the analytical expressions of the resulting coupling matrix elements as well as the breakup cross sections are derived.

The convergence of the angular-distributions breakup cross section is first checked against various numerical parameters that are used in the numerical solution of the coupled differential equations. The stability of the numerical calculations is further tested by comparing the numerical results with the available experimental data.

Comparison of breakup cross section with the total fusion cross section, it is reported that for incident energies below the Coulomb barrier, the breakup cross section is more important than the total fusion cross section. This observation has also been reported in the breakup of the proton-halo ^{8}B on the same target nucleus, in a similar incident energy range. It is found that this importance of the breakup cross section over its fusion counterpart is due to a strong enhancement of the breakup cross section by the continuum-continuum couplings. These couplings are otherwise known to strongly suppress the breakup cross section for incident energies above the Coulomb barrier.

In order to further probe the enhancement of the breakup cross section by the continuum-continuum couplings, the effect of these couplings on its Coulomb and nuclear breakup components is analysed. It is shown that at sub-barrier incident energies, the continuum-continuum couplings strongly enhance the Coulomb breakup cross section, whereas they strongly suppress the nuclear breakup cross section. It followed that the enhancement of the total breakup cross section by these couplings comes exclusively from its Coulomb component. The argument is that the enhancement of the Coulomb breakup cross section below the Coulomb barrier by the continuum-continuum couplings can be explained by

the projectile breakup on its outgoing trajectory. A dominant breakup channel over other reaction channels at deep sub-barrier energies could be comprehensive to breakup of weakly-bound systems and may be justified by the projectile breakup on its outgoing trajectory.

A paper manuscript based on these results has been submitted for review in the journal of European Physical Letters.

Keywords

Neutron-halo nucleus, Discretized continuum coupled-channels, Breakup cross section, Fusion cross section, Continuum-continuum couplings, Coulomb barrier.

Contents

List of Tables

List of Figures

Chapter 1

Introduction

1.1 Background

The studies of the atomic nucleus can be traced back to the early 20th century, when the famous Rutherford experiment was conducted by Geiger and Marsden. Motivated by that experiment, tremendous progress have been made in order to understand nuclear properties from both theoretical and experimental aspects. The atomic nucleus as basic constituent of matter, provides a unique opportunity to study the competition between strong, weak and electromagnetic forces. Therefore, understanding the nuclear structure and reaction mechanisms is critical to other fields, ranging from natural science to human science.
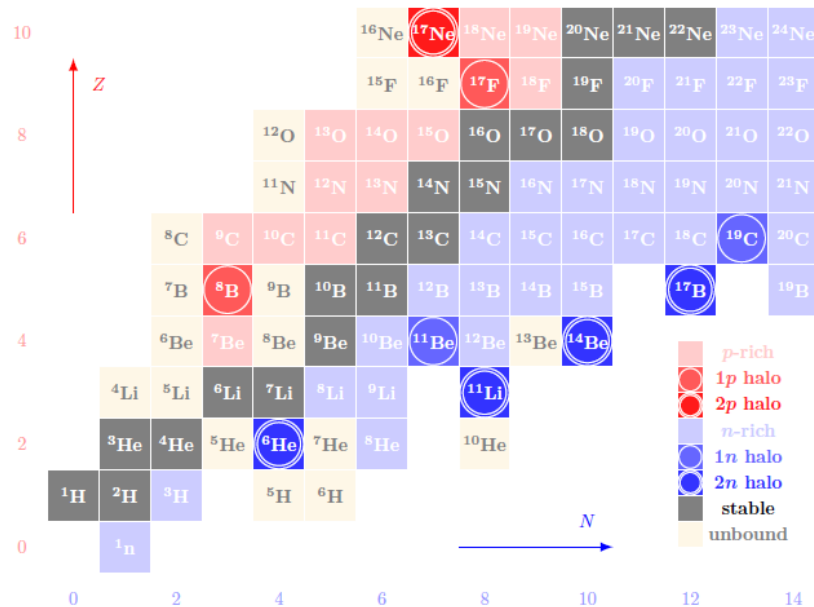
Figure 1.1: Nuclear chart of weakly-bound two and three-body neutron and proton halo nuclei.

It is well-known that the chemical properties of an atom are mainly determined by its atomic number (number of proton) Z. However, isotopes with different number of neutrons N may exhibit different properties. Such isotopes become more and more unstable as the number of neutrons increases. As a result, beyond the neutron and proton driplines on the nuclear chart (see Figure 1.1), no isotopes can be bound. Consequently, of more than three thousand identified nuclei, only a few hundred are known to be stable, having a half-life longer than their natural existence. The remaining ones are referred to as exotic nuclei, meaning that they are artificially produced and characterized. This process is done in Radioactive Ion Beam (RIB) facilities, and hundreds of these facilities have been set up around the world, with advanced equipment designed to produce and detect exotic nuclei. Owing to these facilities, the nuclear chart is being expanded to included more super-heavy elements. Since the discovery of exotic nuclei [1], the study of halo and other loosely-bound nuclei remains one of the most attractive subjects in nuclear physics as exemplified by Refs [2–88] among others. Quantum halos are considered as systems dominated with a few-body structure where nuclear larger radii than the size of the classically allowed regions [89, 90]. As such, a halo system is defined as a compact cloud of nucleons, the so-called core nucleus to which one, two or more nucleons (proton or neutron) are weakly-bound. Due to the effect of the centrifugal barrier, nuclear halos occur in states with low angular momentum ($\ell = 0, 1$) [2], such that halo systems are defined as s-state or p-state systems. Some of the well-known halo systems are ^{8}B (^{7}Be $+ p$), ^{11}Be (^{10}Be $+ n$), ^{19}C (^{18}C $+ n$). These are two-body halo systems since they are formed by a core nucleus with one valence nucleon. When the valence nucleon is a proton, the system is referred to as a proton-halo and when the valence nucleon is a neutron, the system is referred to as a neutron-halo. Therefore, ^{8}B is a proton-halo system, whereas ^{11}Be and ^{19}C are neutron-halo systems. When the core nucleus is surrounded by two nucleons, we have a three-body halo system, such as ^{6}He (^{4}He $+ n + n$) , ^{16}Be (^{14}Be $+ n + n$), ^{22}C (^{20}C $+ n + n$), among others. A three-body system is called *Borromean* if none of its three two-body sub-systems is bound.

1.2   Statement of the problem and motivation

Because of their weak binding energies (low breakup threshold), weakly-bound nuclei break up easily when they come in contact with a target nucleus, or if it enters a Coulomb field of a heavy target nucleus. Consequently, breakup reactions, where a weakly-bound nucleus is dissociated into its constituent fragments, are considered to be one of the adequate tools to probe the structures of weakly-bound systems. The study of effect of the breakup channel on other reaction channels such as elastic scattering, fusion, among others, is the most interesting subject in this field, for example see Refs. [4–17], and references therein. The breakup process of a weakly-bound projectile is mainly caused by two main sources: Coulomb and nuclear forces, leading to Coulomb and nuclear breakups. Despite a spectacular progress in the study of both Coulomb and nuclear breakups over the past few decades, several questions are yet to be fully elucidated. For example: how do the Coulomb and nuclear forces interfere to produce the total breakup? What is the role of the Coulomb-nuclear interference in the breakup process? Which of the Coulomb and nuclear breakups is more dominated by couplings among the projectile continuum states (continuum-continuum couplings)? How do couplings to breakup channels suppress the Coulomb-nuclear interference peak in the elastic scattering cross section?

Studies in this field are mainly focused on incident energy around and above the Coulomb barrier. A recent experimental measurement of the breakup of ^{8}B system on a lead target at deep sub-barrier energies by Pakou *et al.*, [21], yielded quite interesting results. The breakup channel is reported to be the main reaction channel at these energies, overtaking the fusion channel. Intuitively one assumes that at deep sub-barrier energies, the reaction should be dominated by reaction channels other than the breakup channel, given the fact that at such energies, the projectile can be expected to breakup in the absorption region, where its fragments have low probability to survive absorption. A subsequent study in Ref. [22], showed that the predominance of the breakup channel over the fusion chan- nel in this incident energy region can be ascribed to couplings among continuum states. These couplings are otherwise known to strongly suppressed the breakup cross section at incident energies above the Coulomb barrier, see for instance Refs. [4, 5, 23–27]. However, in Ref. [22], it is reported that these couplings rather enhance the breakup cross section

3

below and around the Coulomb barrier and that could be the main reason the breakup channel becomes dominant in this incident energy region. It is further suggested in that reference, that this enhancement could signal a projectile breakup on the outgoing trajectory. Whether the projectile breaks up on its incoming trajectory towards the target or on its outgoing trajectory as it leaves the target and how does that affect the breakup dynamics remains an open question. A following analysis of the same reaction in Ref. [95], within the same incident energy range, further confirmed the findings of Ref. [21], by indicating the effect of Coulomb polarization in the proton halo case, with the correlation information revealing that the prompt breakup mechanism is dominant, occurring predominantly on the outgoing trajectory. This assertion corroborates the suggestion anticipated in Ref. [22] on the breakup of the projectile on the outgoing trajectory.

The results in Refs. [21,22,95], deserve further investigation in order to better understand the breakup dynamics at deep sub-barrier energies. For example, does the enhancement of the breakup cross section by the continuum-continuum couplings at sub-barrier energies come from the Coulomb or nuclear component? An answer to this question could be a further step towards an understanding of the breakup on the outgoing trajectory. Related to the competition between the breakup and fusion channels below the Coulomb barrier, it was also shown in Refs. [54, 94], that the breakup cross section is dominant over the fusion cross section for a heavy target, by considering the ^{6}Li as the projectile (treated as a weakly-bound cluster of an alpha particle and a deuteron), on a lead target.

The results reported in Refs. [21, 22, 95], were obtained for a proton-halo projectile. In order to test their universality, one would consider the neutron-halo projectile as well. The fundamental difference between proton- and neutron-halos is the presence of the Coulomb interaction in the core-proton system that creates a Coulomb barrier within the system, which is absent in the core-neutron system since the neutron is not charged. The Coulomb barrier serves confine the valence proton in the neighbourhood of the core nucleus, as opposed to the neutron-halo case. Therefore, the neutron is expected to be located at a larger distance from its core, compared to the proton, such that the neutron-halo ground state wave function exhibits a longer tail compared to the proton-halo ground state wave function for comparable proton-halo and neutron-halo ground-state

binding energies. Given the asymptomatic nature of the breakup process, the neutron-halo breakup cross section is then expected to be larger in magnitude compared to the proton-halo breakup cross section. It is therefore important to verify whether the Coulomb barrier in the core-proton system has anything to do with the importance of breakup channel over other reaction channels at sub-barrier incident energies, by performing a similar study with a neutron-halo projectile. Such study would also serve to generalize the results of Refs. [21, 22, 95].

1.3 Aims and objectives of the study

The main objective of the present study is to extend the study in Refs. [21, 22, 95], to a neutron-halo system in an effort to test their universality. To this end, we consider the breakup of the ^{11}Be neutron-halo projectile on a lead target, at incident energies below and around the Coulomb barrier. We aim to verify whether for nucleus, where there is no Coulomb barrier between the core nucleus and the valence neutron, the breakup cross section is more important than the total fusion cross section at sub-barrier incident energies. Therefore, this study will implicitly reveal the role of the core-proton Coulomb barrier on the results in Ref. [21, 22, 95], in order to better understand the breakup dynamics at deep sub-barrier energies. In order to extend the study of Ref. [22], we will consider the effect of the couplings among continuum states on the Coulomb and nuclear breakup cross sections at sub-barrier incident energies. We will also investigate whether at sub barrier incident energies the breakup of the projectile nucleus occurs on its incoming or outgoing trajectory. The ^{11}Be nucleus is a well-known one-neutron halo nucleus [7, 90, 105, 106] and have been extensively investigated, both theoretically and experimentally, as evidenced by Refs. [4, 7, 10, 16, 26, 29, 36, 37, 41, 59, 64, 105, 107, 108].

The ^{11}Be nucleus, being the lightest established one neutron-halo system, is a suitable candidate in the attempt to extend the study of the ^{8}B proton-halo system to its neutron-halo counterpart, given the fact that their masses and charges are comparable. However, a study of the relevance of the projectile charge and mass on the breakup cross section is reported in Ref. [3, 94]. It is shown in Ref. [3], that two neutron-halo systems with equivalent ground-state structures, account for different breakup cross sections in mag-

nitude, due to a difference of only one unit in their electric charges. In Ref. [94], it is found that actually the charge and mass of the projectile nucleus could account to similar effects on the breakup cross sections. Again, if the present study proves that the breakup cross section remains larger than the total fusion cross section at incident energies below the Coulomb barrier, that would imply that the charge and atomic mass of the projectile might have limited effect on this feature.

1.4 Methodology

To study the breakup reactions involving weakly-bound projectiles can prove to be a challenging task, in particular from a numerical point of view. The reason is that as already mentioned elsewhere, these reactions are characterized by strong couplings among continuum states of the projectile nucleus. The continuum-continuum couplings matrix elements contain an integration over a product scattering wave functions, which are not square-integrable, making such integration highly oscillatory. As a result, the matrix elements of the continuum-continuum couplings cannot converge and even so for the breakup observables. Such problem is addressed by the continuum discretized coupled-channel (CDCC) method [91–93]. Within this method, the projectile's infinite continuum is truncated subject to convergence requirements, and the continuum wave functions are transformed into square-integrable bin wave functions. This leads to the convergence of the radial integral of the continuum-continuum couplings matrix elements. This method also accurately includes the continuum-continuum couplings in the coupling matrix elements, and it treats the Coulomb and nuclear breakups on the same footing. Its other advantage is that it takes into account multipole excitations as well as the final state interaction effects. As such, this method is known to be the most adequate theoretical tool to probe breakup reactions induced by weakly-bound projectiles. It is therefore the method that we also adopt in the present work. For the sake of simplicity, we will not take into account any target excitations other than those induced by the projectile-target optical potentials. Upon the expansion of projectile-target wave function on the projectile internal states (bound and continuum states), a discretized set of coupled differential equations will be obtained. These equations are transformed into an eigen-value problem

which can be solved iteratively [114, 115]. By imposing the appropriate boundary scattering conditions, the scattering matrix elements are obtained, from which the breakup observables are derived. The stability of our numerical calculations will be tested by analysing the convergence of the breakup cross sections against various parameters such as the the projectile continuum orbital angular momenta, among others. A detailed analysis of the projectile internal structure will be considered given its paramount importance in the breakup process.

1.5   Structure of the Dissertation

This dissertation is structured in the following order: in Chapter 2, we discuss the basic theory of two-body halo systems as well as the Continuum Discretized Couple Channel (CDCC) method. Chapter 3 covers the theoretical description of the three-body scattering systems. The three-body wave function is expanded on the bound-state and bin states of the projectile nucleus, leading to a set of coupled differential equations. In Chapter 4, the details of the numerical calculations are described. The results are presented and discussed in Chapter 5, whereas the conclusion remarks are reported in Chapter 6.

Chapter 2

Theoretical description of two-body bound and scattering states

This chapter, outline the theoretical description of two-body bound- and scattering states. The Hamiltonian of the system and the Schrödinger equation describing the relative motion of the system, as well as the associated boundary conditions are discussed. We are considering a system consisting of a core nucleus (denoted "c"), and a valence nucleon (denoted "v"). In a general description, the spin of the core nucleus is denoted by $\boldsymbol{I}$, and $\boldsymbol{s}$ denotes the spin of the valence nucleon. The relative motion of the core-nucleon system is denoted by $\boldsymbol{r}$, which will be referred to as the projectile internal coordinate in chapter 3. The Schrödinger equation describing the relative motion of the two body-system is given by

$$H_{cv}\phi(\boldsymbol{r}) = \varepsilon_{cv}\phi(\boldsymbol{r}), \tag{2.1}$$

where $\phi(\boldsymbol{r})$, is the wave function, ε_{cv} the total energy

$$\begin{cases} \varepsilon_{cv} < 0 & \text{bound state,} \\ \\ \varepsilon_{cv} > 0 & \text{scattering states,} \end{cases} \tag{2.2}$$

and H_{cv}, is the two-body Hamiltonian defined as

$$H_{cv} = \widehat{T}_{\boldsymbol{r}} + V_{cv}(r), \tag{2.3}$$

with $V_{cv}(r)$, the core-nucleon interacting potential, and $\widehat{T}_{\boldsymbol{r}}$, the kinetic energy operator which is defined as follows

$$\widehat{T}_{\boldsymbol{r}} = -\frac{\hbar^2}{2\mu_{cv}}\nabla_{\boldsymbol{r}}^2, \tag{2.4}$$

where μ_{cv}, is the core-nucleon reduced mass, it is given by

$$\mu_{cv} = \frac{m_c m_v}{m_c + m_v}, \tag{2.5}$$

with m_c, m_v, being the respective atomic masses the core nucleus and valence nucleon, and $\nabla_{\boldsymbol{r}}^2$ the nabla operator is defined, in spherical coordinates (r, θ_r, ϕ_r) as

$$\nabla_{\boldsymbol{r}}^2 = \frac{1}{r^2}\frac{\partial}{\partial r}\left(r^2\frac{\partial}{\partial r}\right) + \frac{1}{r^2\sin^2\theta_r}\frac{\partial}{\partial\theta_r}\left(\sin\theta_r\frac{\partial}{\partial\theta_r}\right) + \frac{1}{r^2\sin^2\theta_r}\frac{\partial^2}{\partial\phi_r^2}. \tag{2.6}$$

If we define the the squared angular momentum operator $\widehat{\boldsymbol{\ell}}^2$ as

$$\widehat{\boldsymbol{\ell}}^2 = -\hbar^2\left[\frac{1}{\sin^2\theta_r}\frac{\partial^2}{\partial\phi_r^2} + \frac{1}{\sin\theta_r}\frac{\partial}{\partial\theta_r}\left(\sin\theta_r\frac{\partial}{\partial\theta_r}\right)\right], \tag{2.7}$$

whose z-projection $\widehat{\boldsymbol{\ell}}_z$ is given by

$$\widehat{\boldsymbol{\ell}}_z = \frac{\hbar}{i}\frac{\partial}{\partial\phi_r}, \tag{2.8}$$

then equation (2.6) becomes,

$$\nabla_{\boldsymbol{r}}^2 = \frac{1}{r^2}\frac{\partial}{\partial r}\left(r^2\frac{\partial}{\partial r}\right) + \frac{\widehat{\boldsymbol{\ell}}^2}{r^2}. \tag{2.9}$$

Substituting equation (2.6), into equation (2.4) the kinetic energy operator becomes

$$\widehat{T}_{\boldsymbol{r}} = -\frac{\hbar^2}{2\mu_{cv}}\left[\frac{1}{r^2}\frac{\partial}{\partial r}\left(r^2\frac{\partial}{\partial r}\right) + \frac{\hat{\boldsymbol{\ell}}^2}{r^2}\right]. \tag{2.10}$$

Taking $V_{cv}(r)$ as a spherical potential, equation (2.6) makes the Hamiltonian H_{cv} to commute with the angular momentum operator $\hat{\boldsymbol{\ell}}$ and its z-projection $\hat{\boldsymbol{\ell}}_z$.

If the internal degrees of freedom of the interacting particles are taken into account, the

wave function $\phi(\boldsymbol{r})$, can be written as

$$\phi(\boldsymbol{r}) = i^\ell \left[[Y_\ell^\nu(\widehat{\boldsymbol{r}}) \otimes \mathcal{X}_s^\mu]_{jm_j} \otimes \mathcal{X}_I^\sigma \right]_{j_{ab}\Lambda} \frac{u_{k\ell}^{j_{ab}}(r)}{r}, \tag{2.11}$$

where $Y_\ell^\nu(\widehat{\boldsymbol{r}})$ is a spherical harmonics [with $\widehat{\boldsymbol{r}} \equiv (\theta_r, \phi_r)$, is the angular part of the coordinate $\boldsymbol{r}$], ν the z-projection of the orbital angular momentum ℓ associated with coordinates $\boldsymbol{r}$], $\mathcal{X}_s^\mu$ is the wave function nucleon's spin (with μ is the z-projection of the nucleon's spin s). To obtain the angular momentum j, we couple the orbital angular momentum ℓ with the spin s ($\boldsymbol{j} = \boldsymbol{\ell} + \boldsymbol{s}$, with $m_j = \nu + \mu$, its z-projection,), $\mathcal{X}_I^\sigma$ is the wave function of the core's spin (with σ the z-projection of I), and j_{ab} is the total angular momentum ($\boldsymbol{j}_{ab} = \boldsymbol{j} + \boldsymbol{I}$), and $\Lambda = m_j + \sigma$ its z-projection. In equation (2.11), $u_{k\ell}^{j_{ab}}(r)$ is the radial part of the wave function, with k the relative wave number defined as

$$k = \sqrt{\frac{2\mu_{cv}\varepsilon_{cv}}{\hbar^2}}. \tag{2.12}$$

The wave function can be identified by the various quantum numbers and write it as

$$\phi_\gamma^\Lambda(\boldsymbol{r}) = i^\ell \sum_{\nu\mu} \sum_{m_j\sigma} \langle \ell\nu s\mu | jm_j \rangle \langle jm_j I\sigma | j_{ab}\Lambda \rangle Y_\ell^\nu(\Omega_{\widehat{r}}) \mathcal{X}_s^\mu \mathcal{X}_I^\sigma \frac{u_{k\ell}^j(r)}{r}, \tag{2.13}$$

where $\gamma \equiv (k, \ell, s, j, I, j_{ab})$ represents a set of quantum numbers that describing a state of the system, $\langle....|..\rangle$ is the Clebsh-Gordon coefficient [101]. For a core nucleus with zero spin ($I = 0$), such that $j_{ab} = j$, $\gamma \equiv (k, \ell, s, j)$, equation (2.13), can be reduced to following simpler form

$$\phi_\gamma^{m_j}(\boldsymbol{r}) = i^\ell \sum_{\nu\mu} \langle \ell\nu s\mu | jm_j \rangle Y_\ell^\nu(\Omega_{\widehat{r}}) \mathcal{X}_s^\mu \frac{u_{k\ell}^j(r)}{r}. \tag{2.14}$$

It can be shown that the radial wave function $u_{k\ell}^j(r)$ satisfies the following differential equation

$$\left[-\frac{\hbar^2}{2\mu_{cv}} \left(\frac{d^2}{dr^2} - \frac{\ell(\ell+1)}{r^2} \right) + V_{cv}(r) \right] u_{k\ell}^j(r) = \varepsilon_{cv} u_{k\ell}^j(r), \tag{2.15}$$

where $\ell(\ell+1)/r^2$, is the centrifugal barrier.

2.1 Boundary conditions

The solution of the differential equation (2.15), requires one to implement the asymptotic appropriate boundary conditions for bound states and scattering states.

2.1.1 Boundary conditions for bound-states

Considering a bound-state, the boundary conditions are such that the wave function $u_{k_b \ell_b}^{j_b}(r)$ is regular at origin $[u_{k_b \ell_b}^{j_b}(r) \to 0, r \to 0$, where ℓ_b and j_b represent the bound state orbital and total angular and k_b the corresponding relative momentum and asymptotically vanishes in the asymptotic region, i.e., $r \to \infty$. That is

$$u_{k_b \ell_b}^{j_b}(r) \overset{r \to \infty}{\Rightarrow} C_{\ell_b, j_b} W_{-\eta_b, \ell_b + \frac{1}{2}}(2k_b r), \tag{2.16}$$

where C_{ℓ_b, j_b}, represents the asymptotic normalization coefficient, and $\eta_b = -i\eta$, the dimensionless Sommerfeld parameter

$$\eta_b = \frac{\mu_{cv}}{\hbar^2} \frac{Z_c Z_v e^2}{k}, \tag{2.17}$$

with Z_c, Z_v, being the numbers of the core nucleus and nucleon ($Z_v = 1$), and $W_{-\eta_b, \ell_b + \frac{1}{2}}(2k_b r)$, the Whittaker function [100], which has the following asymptotic form

$$W_{-\eta_b, \ell_b + \frac{1}{2}}(2k_b r) \overset{r \to \infty}{\Rightarrow} e^{-k_b r + \eta_b \ln(2k_b r)}, \tag{2.18}$$

with η_b and k_b given by

$$\eta_b = \frac{-i Z_c Z_v e^2 \mu_{cv}}{\hbar^2 k_b}, \quad k_b = i\sqrt{\frac{-2\mu_{cv}\varepsilon_{cv}}{\hbar^2}}, \tag{2.19}$$

where $\varepsilon_{cv} < 0$, is the binding energy. If the nucleon is a neutron ($Z_v = 0$), then $\eta_b = 0$, and equation (2.20) reduces to

$$u_{k_b \ell_b}^{j_b}(r) \overset{r \to \infty}{\Rightarrow} C_{\ell_b j_b} e^{-k_b r}. \tag{2.20}$$

The bound-states are normalized according to

$$\int_0^\infty |u_{k_b \ell_b}^{j_b}(r)|^2 dr = 1, \qquad (2.21)$$

and fulfill the following orthogonality relation

$$\langle u_{k_b \alpha_b}(r) | u_{k_b \alpha_b'}(r) \rangle = \delta_{\alpha_b \alpha_b'}, \qquad (2.22)$$

where $\alpha_b = (\ell_b, s, j_b)$ is a set of bound-state quantum numbers describing the projectile bound-state.

2.1.2 Boundary conditions for scattering states

Considering scattering states, the wave function remains regular at the origin, and is asymptotically normalized according to

$$u_{k\ell}^j(r) \overset{r \to \infty}{\longrightarrow} F_\ell(\eta, kr) \cos \delta_{\ell j}(k) + G_\ell(\eta, kr) \sin \delta_{\ell j}(k), \qquad (2.23)$$

where $\delta_{\ell j}(k)$, represents the nuclear phase shift, and $F_\ell(\eta, kr)$ and $G_\ell(\eta, kr)$ are regular and irregular Coulomb functions [114], with the following asymptotic behaviour

$$F_\ell(\eta, kr) \overset{r \to \infty}{\longrightarrow} \sin \left[kr - \eta \ln(2kr) - \frac{\ell \pi}{2} + \sigma_\eta^\ell(k) \right],$$

$$G_\ell(\eta, kr) \overset{r \to \infty}{\longrightarrow} \cos \left[kr - \eta \ln(2kr) - \frac{\ell \pi}{2} + \sigma_\eta^\ell(k) \right], \qquad (2.24)$$

where $\sigma_\eta^\ell(k)$, represents the Coulomb phase shift and it is defined as

$$\sigma_\eta^\ell(k) = \arg \Gamma(1 + \ell + i\eta), \quad \eta = \frac{\mu_{cv} Z_c Z_v e^2}{\hbar^2 k} \qquad (2.25)$$

with $\Gamma(x)$, the Gamma function. Again, in the case of a valence neutron, the Coulomb functions are reduced to spherical Bessel functions $j_\ell(kr)$ and $n_\ell(kr)$, with

$$j_\ell(kr) \overset{r\to\infty}{\Rightarrow} \sin\left(kr - \frac{\ell\pi}{2}\right),$$

$$n_\ell(kr) \overset{r\to\infty}{\Rightarrow} \cos\left(kr - \frac{\ell\pi}{2}\right), \tag{2.26}$$

and they are generally defined as

$$
\begin{aligned}
j_\ell(kr) &= (-r)^\ell \left(\frac{1}{r}\frac{d}{dr}\right)^\ell \frac{\sin(r)}{r}, \\
n_\ell(kr) &= -(-r)^\ell \left(\frac{1}{r}\frac{d}{dr}\right)^\ell \frac{\cos(r)}{r}.
\end{aligned} \tag{2.27}
$$

In such a case equation (2.23) becomes,

$$u_{k\ell}^j(r) \overset{r\to\infty}{\Rightarrow} \sin\left(kr - \frac{\ell\pi}{2} + \delta_{\ell j}(k)\right). \tag{2.28}$$

Considering an s-state, equation (2.29), becomes

$$u_{k\ell}^j(r) \overset{r\to\infty}{\Rightarrow} \sin\left(kr + \delta_{\ell j}(k)\right). \tag{2.29}$$

Although scattering wave functions are not square-integrable, they are known to satisfy the following orthogonality relation

$$\left\langle u_{k\ell}^j(r) | u_{k'\ell'}^{j'}(r) \right\rangle = \delta(k - k')\delta_{\ell\ell'}\delta_{jj'}, \tag{2.30}$$

where $\delta_{aa'}$, is the delta function. Scattering states are orthogonal to bound states, i.e.,

$$\left\langle u_{k\ell}^j(r) | u_{k_b\ell_b}^{j_b}(r) \right\rangle = 0. \tag{2.31}$$

For an accurate description of the breakup process, the exact scattering wave function $\psi_{k\nu\mu}^{+}(\boldsymbol{k}, \boldsymbol{r})$, is needed which is obtained by the following expression

$$\psi_{k\nu\mu}^{+}(\boldsymbol{r}) \rightarrow \frac{1}{(2\pi)^{3/2}}\left[e^{i\boldsymbol{k}\cdot\boldsymbol{r}} + f(\Omega)\frac{e^{ikr}}{r}\right], \tag{2.32}$$

where $e^{i\boldsymbol{k}\cdot\boldsymbol{r}}$, represents the the incoming plane wave, $f(\Omega)$ the scattering amplitude, and $\dfrac{e^{ikr}}{r}$, the outgoing spherical wave. Following Ref. [55], we can expand the wave function $\psi_{k\nu\mu}^{+}(\boldsymbol{r})$, as follows

$$\psi_{k\nu\mu}^{+}(\boldsymbol{r}) \rightarrow \frac{1}{(2\pi)^{3/2}}\sum_{\gamma}C_{\gamma}\phi_{\gamma}^{m_j}(\boldsymbol{r}), \tag{2.33}$$

where the coefficient C_{γ} is defined as

$$C_{\gamma} = \frac{4\pi}{kr}e^{i\delta_{\ell}(k)+\sigma_{\ell}(k)}\sum_{\nu\mu}\langle \ell\nu s\mu|jm_j\rangle Y_{\ell}^{\nu\star}(\Omega_{\boldsymbol{k}}), \tag{2.34}$$

where $\sigma_{\ell}(k)$ is the Coulomb phase shift, given by equation (2.25).

2.2   Discretization of the continuum

Unlike the bound-state, scattering states are infinite, and scattering wave functions are actually not square-integrable. As we have indicated in the introduction, this non square-integrability poses a serious challenge to any numerical treatment of an integral that involves two scattering wave function. Within the Continuum Discretized Couple Channel (CDCC) formalism, the scattering wave function is reduced to a set of discretized bin wave functions that are square-integrable. Being square-integrable, they almost exhibit similar asymptotic behaviour as bound-state wave functions. Two different techniques are commonly used to obtain the bin wave function. The binning technique [92, 114] and the pseudo-state technique [66]. It has been shown in Ref [66, 92], that these two techniques produce equivalent results. In either techniques, the orbital angular momentum ℓ is truncated by $\ell_{\max}$, and the continuous relative momentum k, is truncated by $k_{\max}$. In the pseudo-state technique, the internal Hamiltonian H_{cv}, of the projectile is diagonalized using some basic functions. For instance, the Lagrange-Legendre functions were used in

Ref. [58]. In the binning technique, which we adopt in this work, the truncated momentum interval $[0, k_{\max}]$ discretized into N_b bins $[k_1, k_2], [k_2, k_3], \ldots [k_{N_b-1}, k_{N_b}]$. The width of each bins is $\Delta k = k_i - k_{i-1}$, with $i = 1, 2, 3, \ldots N_b$), and averaged over the relative momentum k [6, 114]. With this technique, the following square integrable bin wave functions $\varphi_\alpha(r)$ are obtained

$$\varphi_\alpha(r) = \sqrt{\frac{2}{\pi W_\alpha}} \int_{k_{i-1}}^{k_i} \mathrm{g}_\alpha(k) u_{k\ell}^j(r) dk, \qquad (2.35)$$

where $\alpha = (i, \ell, s, j)$ stands for the set of quantum numbers which describe the bin states, $\mathrm{g}_\alpha(k)$, the weight function and W_α, is the normalization coefficient which is defined as

$$W_\alpha = \int_{k_{i-1}}^{k_i} |\mathrm{g}_\alpha(k)|^2 dk. \qquad (2.36)$$

The wave function $\varphi_\alpha(r)$ is normalized according to

$$\langle \varphi_\alpha(r) | \varphi_{\alpha'}(r) \rangle = \delta_{\alpha\alpha'}. \qquad (2.37)$$

The bin energies ε_α given by [114]

$$\varepsilon_\alpha = \frac{\hbar^2}{2\mu_{cv} W_\alpha} \int_{k_{i-1}}^{k_i} k^2 |\mathrm{g}_\alpha(k)|^2 dk. \qquad (2.38)$$

The choice of the weight function $\mathrm{g}_\alpha(k)$ is based on the bin's state. For non s-state wave and non-resonant bins, $\mathrm{g}_\alpha(k) = 1$, such that

$$W_\alpha = \int_{k_{i-1}}^{k_i} dk = k_i - k_{i-1} = \Delta k_i. \qquad (2.39)$$

In that case, the bin energies are

$$
\begin{aligned}
\varepsilon_\alpha &= \frac{\hbar^2}{2\mu_{cv}\,W_\alpha} \int_{k_{i-1}}^{k_i} k^2 |\mathrm{g}_\alpha(k)|^2 dk \\
&= \frac{\hbar^2}{2\mu_{cv}\,W_\alpha} \int_{k_{i-1}}^{k_i} k^2 dk \\
&= \frac{\hbar^2}{2\mu_{cv}\,W_\alpha} \times \frac{1}{3} \left[k^3 \right]_{k_{i-1}}^{k_i} \\
&= \frac{\hbar^2}{2\mu_{cv}\,W_\alpha} \times \frac{1}{3} \left(k_i^3 - k_{i-1}^3 \right) \\
&= \frac{\hbar^2}{2\mu_{cv}\,W_\alpha} \times \frac{1}{3} \left(k_i - k_{i-1} \right) \left(k_i^2 + k_i k_{i-1} + k_{i-1}^2 \right) \\
&= \frac{\hbar^2}{2\mu_{cv}} \times \frac{1}{3} \left(k_i^2 + k_i k_{i-1} + k_{i-1}^2 \right).
\end{aligned}
\tag{2.40}
$$

For s-wave bins, it is convenient to set $\mathrm{g}_\alpha(k) = k$. This choice is useful in stabilizing the extraction of the three-body transition amplitude [6,114]. In that case, the normalization coefficient becomes

$$
\begin{aligned}
W_\alpha &= \int_{k_{i-1}}^{k_i} k^2 dk = \frac{1}{3} \left(k_i^3 - k_{i-1}^3 \right) \\
&= \frac{\Delta k_i}{3} \left(k_i^2 + k_{i-1}^2 + k_i k_{i-1} \right),
\end{aligned}
\tag{2.41}
$$

and the bin energies are then given by

$$
\begin{aligned}
\varepsilon_\alpha &= \frac{\hbar^2}{2\mu_{cv}} \frac{1}{W_\alpha} \int_{k_{i-1}}^{k_i} k^4 dk \\[2ex]
&= \frac{\hbar^2}{2\mu_{cv}} \times \frac{1}{5W_\alpha}(k_i^5 - k_{i-1}^5) \\[2ex]
&= \frac{\hbar^2}{2\mu_{cv}W_\alpha} \times \frac{1}{5}\bigg((k_i - k_{i-1})(k_i^4 + k_i^3 k_{i-1} + k_i^2 k_{i-1}^2 + k_i k_{i-1}^3 + k_i^4) \bigg) \\[2ex]
&= \frac{\hbar^2}{2\mu_{cv}W_\alpha} \times \frac{\Delta k_i}{5}\bigg(k_i^4 + k_i^3 k_{i-1} + k_i^2 k_{i-1}^2 + k_i k_{i-1}^3 + k_i^4 \bigg) \\[2ex]
&= \frac{\hbar^2}{2\mu_{cv}} \times \frac{3\Delta k_i}{5\Delta k_i}\bigg(\frac{k_i^4 + k_i^3 k_{i-1} + k_i^2 k_{i-1}^2 + k_i k_{i-1}^3 + k_i^4}{k_i^2 + k_i k_{i-1} + k_{i-1}^2} \bigg) \\[2ex]
&= \frac{\hbar^2}{2\mu_{cv}} \times \frac{3}{5}\bigg(\frac{k_i^4 + k_i^3 k_{i-1} + k_i^2 k_{i-1}^2 + k_i k_{i-1}^3 + k_i^4}{k_i^2 + k_i k_{i-1} + k_{i-1}^2} \bigg).
\end{aligned}
\tag{2.42}
$$

For resonant bins, we follow [27], and write the weight function as

$$
g_\alpha(k) = \left| \frac{\frac{i}{2}\Gamma}{\varepsilon_\alpha - E_r + \frac{i}{2}\Gamma} \right|,
\tag{2.43}
$$

where the resonance width Γ is given by equation (2.44) and the phase shifts $\delta_{\ell j}(k)$ is also used to define the resonance state parameters

$$
\Gamma = 2\left[\frac{\partial}{\partial \varepsilon} \cot \delta_{\ell j} \right]^{-1}.
\tag{2.44}
$$

2.3   Core-nucleon interacting potentials

The core-nucleon potential $V_{cv}(r)$, is an important input that enters into the Schrödinger equation. The general form of this potential is the following

$$
V_{cv}(r) = V_{cv}^{nucl}(r) + V_{cv}^{coul}(r) + V_{cent}(r),
\tag{2.45}
$$

where $V_{cv}^{nucl}(r)$, is the nuclear component, $V_{cv}^{coul}(r)$, the Coulomb component, and $V_{cent}(r)$, the centrifugal component. The nuclear component is defined as

$$V_{cv}^{nucl}(r) = V_0^{nucl}(r) + V_{\text{SO}}^{nucl}(r), \tag{2.46}$$

where $V_0^{nucl}(r)$, represents the central part and $V_{\text{SO}}^{nucl}(r)$, the spin-orbit coupling part. The literature offers a variety of form factors of the nuclear potential, one of the popular ones is the Woods-Saxon form factor, where $V_0^{nucl}(r)$ and $V_{\text{SO}}^{nucl}(r)$ are defined as

$$
\begin{aligned}
V_0^{nucl}(r) &= \frac{V_0}{\left[1 + \exp\left(\frac{r-R_0}{a_0}\right)\right]} \\[2mm]
V_{\text{SO}}^{nucl}(r) &= \left(\frac{\hbar}{m_\pi c}\right)^2 \frac{(\boldsymbol{\ell} \cdot \boldsymbol{s})}{r} \frac{d}{dr} \frac{V_{\text{SO}}}{\left[1 + \exp\left(\frac{r-R_{\text{SO}}}{a_{\text{SO}}}\right)\right]} \\[2mm]
&= -\left(\frac{\hbar}{m_\pi c}\right)^2 \frac{(\boldsymbol{\ell} \cdot \boldsymbol{s})V_{\text{SO}}}{r} \frac{\exp\left(\frac{r-R_{\text{SO}}}{a_{\text{SO}}}\right)}{a_{\text{SO}}\left[1 + \exp\left(\frac{r-R_{\text{SO}}}{a_{\text{SO}}}\right)\right]^2},
\end{aligned}
\tag{2.47}
$$

V_0 (in MeV) is depth of the central part, and V_{SO} (in MeV $\cdot$ fm^2), is depth of the spin-orbit coupling part, (R_x, a_x) $[x \equiv (0, \text{SO})]$ are the corresponding radii and diffuseness, respectively, $\left(\frac{\hbar}{m_\pi c}\right)^2 \simeq 2\,\text{fm}^2$, and the spin-coupling factor is $\boldsymbol{\ell} \cdot \boldsymbol{s} = [j(j+1) - \ell(\ell+1) - s(s+1)]/2$. From equation (2.47), we can see that the the potential $V_{cv}^{nucl}(r)$ vanishes for large values of r, and in fact, this occurs when $r \geq R_x$. This reflects the short-range character of the nuclear potential, owing to the short-range nature of nuclear forces.

As for the Coulomb potential, we consider it to be a point-like sphere, and it is given by

$$
V_{cv}^{coul}(r) =
\begin{cases}
\frac{Z_c Z_v e^2}{R_C}\left(\frac{3}{2} - \frac{r^2}{2R_C^2}\right) & r \leq R_C, \\[4mm]
\frac{Z_c Z_v e^2}{r} & r > R_C,
\end{cases}
\tag{2.48}
$$

where R_C, represents the Coulomb radius. The centrifugal component is given by

$$V_{cv}^{cent}(r) = \frac{\ell(\ell+1)}{r^2},$$ (2.49)

and does not exist for an s-state.

In this chapter, we have described the fundamental basis of two-body systems where we considered bound and scattering states. Boundary conditions in each case were discussed boundary conditions. The two-body potential, which is a crucial input in the numerical evaluation of the two-body Schrödinger equation is also discussed. The basis of the CDCC method, where the scattering wave functions are transformed into square-integrable bin wave functions has also been outlined. In chapter 3, we focus on the dynamics of the three-body system, where the two-body described in this chapter will serve as the projectile nucleus.

Chapter 3

Scattering of three-body systems

3.1 Description of a three-body system

In chapter 2, the fundamentals of a two-body problem are discussed, where two-body bound and scattering states are described. Although the description is valid for any two-body system, we assumed that the system is composed of a core nucleus and valence nucleon. In this chapter, we are going to identify such two-body system as the projectile nucleus (p) which is scattered off a target nucleus (t). In that case, when such projectile interacts with the target one obtains a three-body system ($c + v + t$). The Jacobi coordinates of this system are represented in figure 3.1. In that figure, $\boldsymbol{R}$ is relative coordinate in the projectile-target center-of-mass , $\boldsymbol{R}_{ct}$ is the core-target coordinate and $\boldsymbol{R}_{vt}$ is the nucleon-target coordinate. The coordinates $\boldsymbol{r}$ and $\boldsymbol{R}$ can be expressed in terms of the particles internal coordinates as follows

$$
\begin{aligned}
\boldsymbol{r} &= \boldsymbol{r}_c - \boldsymbol{r}_v, \\
\boldsymbol{R} &= \boldsymbol{r}_t - \frac{m_c \boldsymbol{r}_c + m_v \boldsymbol{r}_v}{m_c + m_v},
\end{aligned}
\tag{3.1}
$$

where $\boldsymbol{r}_v$, $\boldsymbol{r}_c$ and $\boldsymbol{r}_t$, are valence nucleon, core nucleus and target nuclei internal coordinates, respectively. The coordinates $\boldsymbol{R}_{ct}$ and $\boldsymbol{R}_{vt}$ are obtained from the relative coordinate $\boldsymbol{r}$ and $\boldsymbol{R}$ as follows

$$
\begin{aligned}
\boldsymbol{R}_{ct} &= \boldsymbol{R} - \frac{m_v}{m_c + m_v} \boldsymbol{r}, \\
\boldsymbol{R}_{vt} &= \boldsymbol{R} + \frac{m_c}{m_c + m_v} \boldsymbol{r}.
\end{aligned}
\tag{3.2}
$$
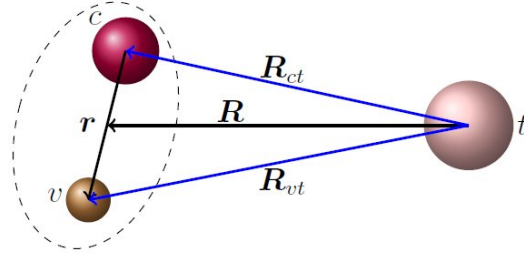
Figure 3.1: Representation of Jacobi coordinates for a the three-body system.

3.2 Schrödinger equation for a three-body system

We consider the three-body wave function $\Psi^{JM}(\boldsymbol{r}, \boldsymbol{R})$ that satisfies the Schrödinger equation

$$(H_{pt} - E)\Psi^{JM}(\boldsymbol{r}, \boldsymbol{R}) = 0, \tag{3.3}$$

where E is the total energy, J, the total angular momentum, (which is constant of motion, with M z-projection of J), and H_{pt} the three-body Hamiltonian defined as

$$H_{pt} = H_{cv} + \widehat{T}_{\boldsymbol{R}} + U_{pt}(\boldsymbol{r}, \boldsymbol{R}), \tag{3.4}$$

where H_{cv}, is the two-body Hamiltonian given by equation (2.3), $\widehat{T}_{\boldsymbol{R}}$, is the kinetic energy operator defined as

$$\widehat{T}_{\boldsymbol{R}} = -\frac{\hbar^2}{2\mu_{pt}}\nabla^2_{\boldsymbol{R}}, \tag{3.5}$$

with μ_{pt}, being the reduced mass of the projectile-target system, and $\nabla^2_{\boldsymbol{R}}$, is the usual nabla operator. In equation (3.4), $U_{pt}(\boldsymbol{r}, \boldsymbol{R})$ is the three-body potential. This potential has two components, namely the core-target potential $U_{ct}(\boldsymbol{R}_{ct})$ and valence-target potential $U_{vt}(\boldsymbol{R}_{vt})$, i.e.,

$$\begin{aligned} U_{pt}(\boldsymbol{r}, \boldsymbol{R}) &= U_{ct}(\boldsymbol{R}_{ct}) + U_{vt}(\boldsymbol{R}_{vt}) \\ &= V_{ct}^{Coul}(\boldsymbol{R}_{ct}) + U_{ct}^{Nucl}(\boldsymbol{R}_{ct}) + V_{vt}^{Coul}(\boldsymbol{R}_{vt}) + U_{vt}^{Nucl}(\boldsymbol{R}_{vt}), \end{aligned} \tag{3.6}$$

where $V_a^{Coul}(\boldsymbol{R}_a)$ and $U_a^{nucl}(\boldsymbol{R}_a)$ are Coulomb and nuclear components ($a = ct, vt$). The nuclear potential contains two parts: a real part and an imaginary one, that is

$$U_{xt}^{nucl}(\boldsymbol{R}_{xt}) = V_{xt}(\boldsymbol{R}_{xt}) + iW_{xt}(\boldsymbol{R}_{xt}), \tag{3.7}$$

where $V_{xt}(\boldsymbol{R}_{xt})$ is the real part and $W_{xt}(\boldsymbol{R}_{xt})$ the imaginary part.

3.3 Expansion of the three-body wave function

The three-body wave function $\Psi_{K_\gamma}^{JM}(\boldsymbol{r}, \boldsymbol{R})$ is expanded on the projectile internal states as follows (considering an inert target nucleus)

$$\Psi_{K_\gamma}^{JM}(\boldsymbol{r}, \boldsymbol{R}) = \sum_{\alpha_b, L} \frac{F_{\alpha_b}^{LJ}(R)}{R} \mathcal{Y}_{\alpha_b}^{LJ}(\boldsymbol{r}, \Omega_{\widehat{\boldsymbol{R}}}) + \sum_{\gamma, L} \int \frac{F_\gamma^{LJ}(R)}{R} \mathcal{Y}_\gamma^{LJ}(\boldsymbol{r}, \Omega_{\widehat{\boldsymbol{R}}}) dR, \tag{3.8}$$

where $F_{\alpha_b}^{LJ}(R)$ and $F_\gamma^{LJ}(R)$, are respectively the radial components of the wave function in the elastic scattering and breakup channels, and $\mathcal{Y}_{\alpha_b}^{LJ}(\boldsymbol{r}, \Omega_{\widehat{\boldsymbol{R}}})$ and $\mathcal{Y}_\gamma^{LJ}(\boldsymbol{r}, \Omega_{\widehat{\boldsymbol{R}}})$ are the corresponding channel wave functions, with $\Omega_{\widehat{\boldsymbol{R}}}$, the angular part of the coordinate $\boldsymbol{R}$ ($\Omega_{\widehat{\boldsymbol{R}}} \equiv (\theta, \phi)$), and K_{α_b} and K_γ are the the initial and final linear momenta. They are related through the conservation of energy

$$\frac{\hbar^2}{2\mu_{pt}} K_\gamma^2 + \varepsilon_\gamma = \frac{\hbar^2}{2\mu_{pt}} K_{\alpha_b}^2 + \varepsilon_{\alpha_b}. \tag{3.9}$$

In Eq(3.8) the channel wave functions are defined as

$$\mathcal{Y}_{\alpha_b}^{LJ}(\boldsymbol{r}, \Omega_{\widehat{\boldsymbol{R}}}) = i^L \left[\phi_{\alpha_b}^{m_{j_b}}(\boldsymbol{r}) \otimes Y_L^{M_L}(\Omega_{\widehat{\boldsymbol{R}}}) \right]_{JM},$$

$$\mathcal{Y}_\gamma^{LJ}(\boldsymbol{r}, \Omega_{\widehat{\boldsymbol{R}}}) = i^L \left[\phi_\gamma^{m_j}(\boldsymbol{r}) \otimes Y_L^{M_L}(\Omega_{\widehat{\boldsymbol{R}}}) \right]_{JM}, \tag{3.10}$$

where $\phi_{\alpha_b}^{m_{j_b}}(\boldsymbol{r})$ is the bound-state wave function identified by equation (2.11) [whose radial part is normalized according to equation (2.20)], and $\phi_\gamma^{m_j}(\boldsymbol{r})$ is the scattering wave function, and its radial part is normalized according to equation (2.23), and $Y_L^{M_L}(\Omega_{\boldsymbol{R}})$, are spherical harmonics, with L, the orbital angular momentum related to relative coordinate $\boldsymbol{R}$. The total angular momentum is then given by $\boldsymbol{J} = \boldsymbol{L} + \boldsymbol{j}$.

In equation ((3.8), first sum runs over the internal bound-states of the projectile and the second sum over the scattering states. For a system with only one bound-state, the first sum has one term. However, due to the infinite number of scattering states, the second sum runs to infinity, and in that case, the wave function (3.8) has an infinite number of terms, leading to numerical intractability. In order to reduce the expansion (3.8) to a finite number of terms for numerical purpose, we apply the CDCC formalism outlined in Section 2.2. To this end, the wave function $\Psi_{K_\gamma}^{JM}(\boldsymbol{r}, \boldsymbol{R})$ is approximated by the following CDCC wave function

$$\Psi_{K_\beta}^{JM}(\boldsymbol{r}, \boldsymbol{R}) = \sum_{\alpha_b, L} \frac{F_{\alpha_b}^{LJ}(R)}{R} \mathcal{Y}_{\alpha_b}^{LJ}(\boldsymbol{r}, \Omega_{\widehat{\boldsymbol{R}}}) + \sum_{\alpha, L} \frac{F_\alpha^{LJ}(R)}{R} \mathscr{Y}_\alpha^{LJ}(\boldsymbol{r}, \Omega_{\widehat{\boldsymbol{R}}}), \qquad (3.11)$$

where the subscript $\beta \equiv (\alpha_b, \alpha)$ reduces to $\alpha_b = (\ell_b, s, j_b)$ in the elastic channel and to $\alpha = (i, \ell, s, j)$ in the breakup channel, and the discretized channel wave function $\mathscr{Y}_\alpha^{LJ}(\boldsymbol{r}, \Omega_{\widehat{\boldsymbol{R}}})$ is given by

$$\begin{aligned}
\mathscr{Y}_\alpha^{LJ}(\boldsymbol{r}, \widehat{\boldsymbol{R}}) &= i^L \left[\Phi_\alpha^{m_j}(\boldsymbol{r}) \otimes Y_L^{M_L}(\Omega_{\widehat{\boldsymbol{R}}}) \right]_{JM} \\
&= i^{\ell+L} \sum_{\nu\mu} \sum_{m_j M_L} \langle \ell\nu s\mu | jm_j \rangle \langle jm_j LM_L | JM \rangle Y_\ell(\Omega_{\widehat{\boldsymbol{r}}}) Y_L(\Omega_{\widehat{\boldsymbol{R}}}) X_s \frac{\varphi_\alpha(r)}{r},
\end{aligned}$$
$$(3.12)$$

with $\Phi_\alpha^{m_j}(\boldsymbol{r})$, being the discretized wave function which contains the bin wave function $\varphi_\alpha(r)$ (2.35).

3.4   Coupled differential equations

The substitution of the expansion (3.11) into the Schrödinger equation, yields the following set of coupled differential equations

$$\left[T_R + V_{\beta\beta}^{LJ}(R) + \varepsilon_\beta - E \right] F_\beta^{LJ}(R) - \sum_{\beta \neq \beta'} i^{L-L'} V_{\beta\beta'}^{L'J}(R) F_{\beta'}^{L'J}(R) = 0, \qquad (3.13)$$

where the kinetic energy term T_R is given by

$$T_R = -\frac{\hbar^2}{2\mu_{pt}}\left[\frac{d^2}{dR^2} - \frac{L(L+1)}{R^2}\right], \tag{3.14}$$

and $V_{\beta\beta}^{LJ}(R)$ and $V_{\beta\beta'}^{LL'J}$ are coupling matrix elements, where $V_{\beta\beta}^{LJ}(R)$, represents the diagonal coupling matrix elements and $V_{\beta\beta'}^{LL'J}$ stands for the off-diagonal coupling matrix elements, with

$$V_{\beta\beta}^{LJ}(R) = V_{\alpha_b\alpha_b}(R) + V_{\alpha\alpha}(R)$$
$$V_{\beta\beta'}^{LL'J}(R) = V_{\alpha_b\alpha'}(R) + V_{\alpha\alpha'}(R). \tag{3.15}$$

In this equation, $V_{\alpha_b\alpha_b}(R)$, is the coupling matrix elements in the elastic scattering channel, $V_{\alpha\alpha}(R)$, is the coupling matrix elements among that couple diagonal continuum states, $V_{\alpha_b\alpha'}(R)$, is the coupling to and from the bound-state, and $V_{\alpha\alpha'}(R)$, is for the off-diagonal continuum-continuum couplings. The coupling matrix elements are given by the following equation

$$\begin{aligned} V_{\beta\beta'}^{LL'J}(R) &= \langle \mathcal{Y}_{\alpha_b}^{LJ}(\boldsymbol{r},\Omega_{\widehat{\boldsymbol{R}}})|U_{pt}(\boldsymbol{r},\boldsymbol{R})|\mathcal{Y}_{\alpha}^{LJ}(\boldsymbol{r},\Omega_{\widehat{\boldsymbol{R}}})\rangle \\[2mm] &+ \langle \mathcal{Y}_{\alpha}^{LJ}(\boldsymbol{r},\Omega_{\widehat{\boldsymbol{R}}})|U_{pt}(\boldsymbol{r},\boldsymbol{R})|\mathcal{Y}_{\alpha'}^{L'J}(\boldsymbol{r},\Omega_{\widehat{\boldsymbol{R}}})\rangle, \end{aligned} \tag{3.16}$$

where the wave function $\mathcal{Y}_{\alpha}^{LJ}(\boldsymbol{r},\widehat{\boldsymbol{R}})$, is given by equation (3.12), and optical potential $U_{pt}(\boldsymbol{r},\boldsymbol{R})$ by equation (3.6).

3.5   Calculation of the coupling matrix elements

To solve the coupled differential equations (3.13), the coupling matrix elements must be evaluated. To this end, the three-body potential $U_{pt}(\boldsymbol{r},\boldsymbol{R})$ first is expanded in potential

multipole with multipole order λ as

$$
\begin{aligned}
U(\boldsymbol{r}, \boldsymbol{R}) &= \sum_{\lambda=0}^{\lambda_{\max}} U_\lambda(r, R) P_\lambda(\cos\theta) \\[2mm]
&= \sum_{\lambda=0}^{\lambda_{\max}} U_\lambda(r, R) \frac{4\pi}{2\lambda+1} \sum_{\vartheta=-\lambda}^{\lambda} Y_\lambda^\vartheta(\Omega_{\widehat{\boldsymbol{r}}}) \cdot Y_\lambda^{\vartheta\star}(\Omega_{\widehat{\boldsymbol{R}}}) \qquad (3.17) \\[2mm]
&= \sum_{\lambda=0}^{\lambda_{\max}} \frac{4\pi}{2\lambda+1} U_\lambda(r, R) Y_\lambda(\Omega_{\widehat{\boldsymbol{r}}}) \cdot Y_\lambda(\Omega_{\widehat{\boldsymbol{R}}}),
\end{aligned}
$$

where $\lambda_{\max}$ is the maximum multipole order, $P_\lambda(\cos\theta)$ are Legendre polynomials, and $U_\lambda(r, R)$ are potential multipole, which we can define as

$$
U_\lambda = \frac{2\lambda+1}{2} \int_{-1}^{1} U_{pt}(\boldsymbol{r}, \boldsymbol{R}) P_\lambda(z) dz, \qquad (3.18)
$$

with $z = \cos\theta$. Substituting the expansion (3.17), into equation (3.16), yields

$$
\begin{aligned}
V_{\alpha\alpha'}(R) &= \left\langle \mathscr{Y}_\alpha^{LJ}(\boldsymbol{r}, \Omega_{\widehat{\boldsymbol{R}}}) \left| \sum_{\lambda=0}^{\lambda_{\max}} \frac{4\pi}{2\lambda+1} U_\lambda(r, R) Y_\lambda(\Omega_{\widehat{\boldsymbol{r}}}) \cdot Y_\lambda(\Omega_{\widehat{\boldsymbol{R}}}) \right| \mathscr{Y}_{\alpha'}^{LJ}(\boldsymbol{r}, \Omega_{\widehat{\boldsymbol{R}}}) \right\rangle \\[2mm]
&= \sum_{\lambda=0}^{\lambda_{\max}} \frac{4\pi}{2\lambda+1} \left\langle \mathscr{Y}_\alpha^{LJ}(\boldsymbol{r}, \Omega_{\widehat{\boldsymbol{R}}}) \left| U_\lambda(r, R) Y_\lambda(\Omega_{\widehat{\boldsymbol{r}}}) \cdot Y_\lambda(\Omega_{\widehat{\boldsymbol{R}}}) \right| \mathscr{Y}_{\alpha'}^{LJ}(\boldsymbol{r}, \Omega_{\widehat{\boldsymbol{R}}}) \right\rangle. \quad (3.19)
\end{aligned}
$$

Substituting equation (3.12) into equation (3.19), one obtains

$$
\begin{aligned}
V_{\alpha\alpha'}(R) &= i^{\ell+\ell'+L+L'} \sum_{\lambda=0}^{\lambda_{\max}} \frac{4\pi}{2\lambda+1} \sum_{\nu\nu'\mu} \sum_{m_j m_{j'} M_L M_{L'}} \langle \ell\nu s\mu | j m_j \rangle \langle j m_j L M_L | J M \rangle \\[2mm]
&\quad \times \langle \ell'\nu' s\mu | j' m_{j'} \rangle \langle j' m_{j'} L' M_{L'} | J M \rangle \langle \ell'\nu' s\mu | \lambda 0 \rangle \langle L M_L L' M_{L'} | \lambda 0 \rangle \qquad (3.20) \\[2mm]
&\quad \times \langle Y_\ell(\Omega_{\widehat{\boldsymbol{r}}}) | Y_\lambda(\Omega_{\widehat{\boldsymbol{r}}}) | Y_{\ell'}(\Omega_{\widehat{\boldsymbol{r}}}) \rangle \langle Y_L(\Omega_{\widehat{\boldsymbol{R}}}) | Y_\lambda(\Omega_{\widehat{\boldsymbol{R}}}) | Y_{L'}(\Omega_{\widehat{\boldsymbol{R}}}) \rangle \langle \varphi_\alpha | U_\lambda(r, R) | \varphi_{\alpha'} \rangle,
\end{aligned}
$$

where according to the properties of spherical harmonics [101], we have

$$
\langle Y_\ell(\Omega_{\widehat{\boldsymbol{r}}})|Y_\lambda(\Omega_{\widehat{\boldsymbol{r}}})|Y_{\ell'}(\Omega_{\widehat{\boldsymbol{r}}})\rangle \;=\; (-1)^\ell \frac{\sqrt{(2\ell+1)(2\lambda+1)(2\ell'+1)}}{\sqrt{4\pi}} \begin{pmatrix} \ell & \lambda & \ell' \\ 0 & 0 & 0 \end{pmatrix},
$$

$$
\langle Y_L(\Omega_{\widehat{\boldsymbol{R}}})|Y_\lambda(\Omega_{\widehat{\boldsymbol{R}}})|Y_{L'}(\Omega_{\widehat{\boldsymbol{R}}})\rangle \;=\; (-1)^L \frac{\sqrt{(2L+1)(2\lambda+1)(2L'+1)}}{\sqrt{4\pi}} \begin{pmatrix} \ell & \lambda & \ell' \\ 0 & 0 & 0 \end{pmatrix}. \tag{3.21}
$$

Since the Clebsch-Gordan coefficients can be written in terms of 3-j symbols, as follows [101]

$$
\langle j_1 m_1 j_2 m_2 | j_3 m_3 \rangle \;=\; (-1)^{-j_1+j_2-m_3}\sqrt{2j_3+1} \begin{pmatrix} j_1 & j_2 & j_3 \\ m_1 & m_2 & -m_3 \end{pmatrix}, \tag{3.22}
$$

and

$$
\begin{pmatrix} j_1 & j_2 & j_3 \\ m_1 & m_2 & m_3 \end{pmatrix} = (-1)^{j_1+j_2+j_3} \begin{pmatrix} j_1 & j_3 & j_2 \\ m_1 & m_3 & m_2 \end{pmatrix}, \tag{3.23}
$$

equation (3.20) becomes,

$$
\begin{aligned}
V_{\alpha\alpha'}(R) &= i^{\ell+\ell'+L+L'} \sum_{\lambda=0}^{\lambda_{\max}} \frac{4\pi}{2\lambda+1} \sum_{\nu\nu'\mu} \sum_{m_j m_{j'} M_L M_{L'}} (-1)^{2s+j-m_j} \sqrt{2j+1}
\begin{pmatrix} \ell & j & s \\ \nu & -m_j & \mu \end{pmatrix} \\
&\times (-1)^{2L+J-M} \sqrt{2J+1}
\begin{pmatrix} j & J & L \\ m_j & -M & M_L \end{pmatrix}
(-1)^{2s+j'-m_{j'}} \sqrt{2j'+1}
\begin{pmatrix} \ell' & j' & s \\ \nu' & -m_{j'} & \mu' \end{pmatrix} \\
&\times (-1)^{2L'+J-M} \sqrt{2J+1}
\begin{pmatrix} j' & J & L' \\ m_{j'} & -M & M_{L'} \end{pmatrix}
(-1)^{2\ell'+\lambda} \sqrt{2\lambda+1}
\begin{pmatrix} \ell & \lambda & \ell' \\ \nu & 0 & \nu' \end{pmatrix} \qquad (3.24) \\
&\times (-1)^{2L'+\lambda} \sqrt{2\lambda+1}
\begin{pmatrix} L & \lambda & L' \\ M_L & 0 & M_{L'} \end{pmatrix}
(-1)^{\ell+L} \frac{\sqrt{(2\lambda+1)(2\ell+1)(2\ell'+1)(2L+1)(2L'+1)}}{4\pi} \\
&\times \begin{pmatrix} \ell & \lambda & \ell' \\ 0 & 0 & 0 \end{pmatrix}
\begin{pmatrix} \ell & \lambda & \ell' \\ 0 & 0 & 0 \end{pmatrix}
\langle \varphi_\alpha | U_\lambda(r,R) | \varphi_{\alpha'} \rangle.
\end{aligned}
$$

Considering the definition of Racah coefficients in terms of the 3-j symbols [101], the following final expression of the coupling matrix elements is obtained

$$
\begin{aligned}
V_{\alpha\alpha'}(R) &= i^{\ell+\ell'+L+L'} \sum_{\lambda=0}^{\lambda_{\max}} (-1)^{J-L-j'+\lambda-L'} \widehat{\ell\ell'}\,\widehat{LL'}\,\widehat{jj'}\,\widehat{J} \\
&\times \begin{pmatrix} \ell & \lambda & \ell' \\ 0 & 0 & 0 \end{pmatrix}
\begin{pmatrix} L & \lambda & L' \\ 0 & 0 & 0 \end{pmatrix}
W(\ell\ell'jj';\lambda s) W(LL'jj';\lambda J) I_{\alpha\alpha'}(R), \quad (3.25)
\end{aligned}
$$

where $W(abcd;ef)$ are Racah coefficients [101], and $I_{\alpha\alpha'}(R)$ is the radial integral given by

$$
I_{\alpha\alpha'}(R) = \int_0^\infty dr\, \varphi_\alpha^\star(r) U_\lambda(r,R) \varphi_{\alpha'}(r), \qquad (3.26)
$$

which is to be evaluated numerically and it is expected to converge owing to the square-integrability of the bin wave functions. This is what makes the CDCC formalism uniquely designed to handle breakup dynamics of weakly-bound systems. If one considers the pure

---

scattering wave functions $u_{k\ell}^j(r)$, the radial integral in this equation will not converge, since the product of two pure scattering wave functions would be highly oscillatory, implying a convergence failure of the coupling matrix elements $V_{\alpha\alpha'}(R)$. We would follow the same procedure to derive the matrix elements for couplings to and from the ground-state $V_{\alpha_b\alpha}(R)$. In the asymptotic region where the projectile and target are far apart $(R \to \infty)$, the nuclear interactions are inactive due to the short-range character of nuclear forces. Then, the potential $U_{pt}(\boldsymbol{r}, \boldsymbol{R})$ is reduced to its Coulomb component. The potential multipole expansion of the Coulomb potential gives [117, 118]

$$V_{pt}^{\text{Coul}}(\boldsymbol{r}, \boldsymbol{R}) \overset{R\to\infty}{\to} 4\pi Z_t e \sum_{\lambda=0}^{\lambda_{max}} \frac{\sqrt{2\lambda+1}}{R^{\lambda+1}} \left[\mathcal{M}_\lambda^\varepsilon(\boldsymbol{r}) \otimes Y_\lambda(\Omega_{\widehat{\boldsymbol{R}}})\right]_{\lambda 0}, \tag{3.27}$$

where $Z_t e$, represents the charge of the target nucleus, and $\mathcal{M}_\lambda^\varepsilon(\boldsymbol{r})$, the core-nucleon electric operator, which is given by

$$\mathcal{M}_\lambda^\varepsilon(\boldsymbol{r}) = Z_\lambda r^\lambda Y_\lambda^\vartheta(\widehat{\boldsymbol{r}}), \tag{3.28}$$

with Z_λ, being the effective charge defined as

$$Z_\lambda = e\left[Z_v\left(\frac{m_c}{m_p}\right)^\lambda + Z_c\left(-\frac{m_v}{m_p}\right)^\lambda\right], \tag{3.29}$$

where $Z_v e$ and $Z_c e$, the respective valence nucleon and core nucleus charges. The continuum-continuum Coulomb coupling matrix elements are given by

$$V_{\alpha\alpha'}^{Coul}(R) = Z_t e \sum_{\lambda=0}^{\lambda_{max}} (-1)^{J-L-j'+\lambda-L'} \sqrt{(2L+1)(2L'+1)(2j'+1)(2J+1)} \begin{pmatrix} L & \lambda & L' \\ 0 & 0 & 0 \end{pmatrix}$$

$$\times \quad W(LL'jj'; \lambda J)\langle\varphi_\alpha(\boldsymbol{r})|Y_\lambda(\Omega_{\widehat{\boldsymbol{r}}})\mathcal{M}_\lambda^\varepsilon(\boldsymbol{r})|\varphi_{\alpha'}(\boldsymbol{r})\rangle I_{\alpha\alpha'}(R). \tag{3.30}$$

In this equation, the radial integral $I_{\alpha\alpha'}(R)$ is defined as

$$I_{\alpha\alpha'}(R) = \int_{R>R_n}^\infty F_L(K_\alpha R)\frac{1}{R^{\lambda+1}}F_{L'}(K_{\alpha'}R)dR, \tag{3.31}$$

with $F_L(x)$, being Coulomb functions [114], and $R_n = r_0(A_p^{1/3} + A_t^{1/3})$. After the are numerically calculation of coupling matrix elements, the coupled differential equations (3.13), are numerically solved with to the following boundary conditions in the asymptotic region

$$F_\beta^{LJ}(R) \overset{R \to \infty}{\to} \frac{\mathrm{i}}{2} \left[H_\beta^-(K_\beta R)\delta_{\alpha_b\alpha} - H_\beta^+(K_\beta R)S_{\beta\beta'}^J(K_{\beta'}) \right], \qquad (3.32)$$

where $H_\beta^\pm(K_\beta R)$, are Coulomb-Hankel functions [114], and $S_{\beta\beta'}^J(K_{\beta'})$ is the scattering S-matrix.

3.6   Breakup cross sections

One can calculate the breakup cross sections by first determining the transition matrix elements among different states of the projectile nucleus. This transition matrix, which we denote by $\mathcal{T}_{\nu\mu}^{m_j}(\boldsymbol{k}, \boldsymbol{K}_\gamma)$, is given by [6, 114]

$$\mathcal{T}_{\nu\mu}^{m_j}(\boldsymbol{k}, \boldsymbol{K}_\gamma) = \left\langle \psi_{k\nu\mu}^{(+)}(\boldsymbol{r})e^{i\boldsymbol{K}_\gamma \cdot \boldsymbol{R}} | U(\boldsymbol{r}, \boldsymbol{R}) | \Psi_{K_\gamma}^{JM}(\boldsymbol{r}, \boldsymbol{R}) \right\rangle, \qquad (3.33)$$

where the $\psi_{k\nu\mu}^{(+)}(\boldsymbol{r})$ is given by equation (2.33), $e^{i\boldsymbol{K}\cdot\boldsymbol{R}}$, is the plane wave describing the projectile-target final state, and the original projectile-target wave function $\Psi_{K_\gamma}^{JM}(\boldsymbol{r}, \boldsymbol{R})$, is given by equation (3.8). For the transition matrix elements $\mathcal{T}_{\nu\mu}^{m_j}(\boldsymbol{k}, \boldsymbol{K}_\gamma)$ to converge, the pure replace the projectile-target wave function is replaced by its CDCC approximation $\Psi_{K_\beta}^{JM}(\boldsymbol{r}, \boldsymbol{R})$, and insert the bin wave functions $\Phi_\alpha^{m_j}(\boldsymbol{r})$ in the bra and ket of equation (3.33) to obtain [6, 114]

$$\mathcal{T}_{\nu\mu}^{m_j}(\boldsymbol{k}, \boldsymbol{K}_\beta) = \sum_\beta \sum_{m_j} s(k)\mathcal{T}_{\nu m_j}^\beta(\boldsymbol{K}_\beta), \qquad (3.34)$$

where

$$\mathcal{T}_{\nu m_j}^\beta(\boldsymbol{K}_\beta) = \left\langle \Phi_\alpha^{m_j}(r) | U(\boldsymbol{r}, \boldsymbol{R}) | \Psi_{K_\gamma}^{JM}(\boldsymbol{r}, \boldsymbol{R}) \right\rangle, \qquad (3.35)$$

and $s(k) = \left\langle \psi_{k\nu\mu}^{(-)}(\boldsymbol{r}) | \Phi_\alpha^{m_j}(\boldsymbol{r}) \right\rangle$, is the so-called smoothing factor, and it is given by [6, 114]

$$
\begin{aligned}
s(k) &= \frac{4\pi}{k} \sum_\alpha (-i)^\ell e^{i[\delta_{\ell j}(k) + \sigma_{\ell j}(k)]} \sum_\nu \langle \ell\nu s\mu | jm_j \rangle Y_\ell^\nu(\widehat{\boldsymbol{k}}) \\
&\times \int \Phi_\alpha^{m_j^\star}(\boldsymbol{k}, \boldsymbol{r}) \phi_\alpha^{m_j}(\boldsymbol{r}) d^3\boldsymbol{r}.
\end{aligned} \tag{3.36}
$$

The projectile final state wave function $\psi_{k\nu\mu}^{(-)}(\boldsymbol{r})$ is obtained through the application of the time-reversal operator [100], on the wave function $\psi_{k\nu\mu}^{(+)}(\boldsymbol{r})$. Considering the orthogonality of the Clebsh-Gordon coefficients and the properties of the spherical harmonics, one obtains

$$
\int \Phi_\alpha^{m_j^\star}(\boldsymbol{k}, \boldsymbol{r}) \Phi_\alpha^{m_j}(\boldsymbol{r}) d^3\boldsymbol{r} = \sqrt{\frac{2}{\pi W_\alpha}} g_\alpha(k) \quad \text{if} \quad k \in [k_{i-1}, k_i], \tag{3.37}
$$

where this integral is zero if $k \notin [k_{i-1}, k_i]$. The factor $s(k)$ becomes

$$
s(k) = \frac{4\pi}{k} \sum_\alpha (-i)^\ell e^{i[\delta_{\ell j}(k) + \sigma_{\ell j}(k)]} \sqrt{\frac{2}{\pi W_\alpha}} \int_{k_{i-1}}^{k_i} dk \, g_i(k) \sum_\nu \langle \ell\nu s\mu | jm_j \rangle Y_\ell^\nu(\widehat{\boldsymbol{k}}). \tag{3.38}
$$

Because the breakup process is generally regarded as an inelastic excitation of the projectile nucleus, the matrix elements $\mathcal{T}_{\nu m_j}^\beta(\boldsymbol{K}_\beta)$ can be expressed in terms of the inelastic scattering amplitude $F_{m_j}^{m_{j'}}(\widehat{\boldsymbol{R}})$ as follows [114]

$$
\mathcal{T}_{\nu m_j}^\beta(\boldsymbol{K}_\beta) = -\frac{2\pi\hbar^2}{\mu_{pt}} \sqrt{\frac{K_{\alpha_b}}{K_\alpha}} F_{m_j}^{m_{j'}}(\widehat{\boldsymbol{R}}), \tag{3.39}
$$

where the amplitude $F_{m_j}^{m_{j'}}(\widehat{\boldsymbol{R}})$, is given by

$$
\begin{aligned}
F_{m_j}^{m_{j'}}(\widehat{\boldsymbol{R}}) &= \frac{\sqrt{\pi}}{iK_{\alpha_b}} \sqrt{\frac{K_\alpha}{K_{\alpha_b}}} \sum_{LL'} \sum_J \sqrt{2L+1} \langle LM_L jm_j | JM_L \rangle \langle L'M_{L'} j'm_{j'} | JM \rangle \\
&\times e^{i(\sigma_L + \sigma_{L'})} S_{\beta\beta'}^J(K_{\beta'}) Y_{L'}^{M_{L'}}(\widehat{\boldsymbol{R}}),
\end{aligned} \tag{3.40}
$$

with $S_{\beta\beta'}^J$ the scattering matrix that appears in equation (3.32), and σ_L, and $\sigma_{L'}$, the Coulomb phase shifts given by

$$\sigma_L = \arg\Gamma(L+1+i\eta_{pt}), \quad \eta_{pt} = \frac{\mu_{pt}Z_pZ_te^2}{\hbar^2 K_{\alpha_b}},$$ (3.41)

Substituting of equations (3.38), (3.40) into equation (3.34) results in the following expression for the breakup transition matrix elements

$$\begin{aligned}
\mathcal{T}_{\nu\mu}^{m_j}(\boldsymbol{k}, \boldsymbol{K}_\beta) &= -\frac{8\pi^{\frac{5}{2}}\hbar^2}{\mu_{pt}}\frac{1}{ikK_{\alpha_b}}\sum_\ell\sum_{jm_j}(-i)^\ell h(k)\sum_\nu \big\langle\,\ell\nu s\mu|jm_j\big\rangle Y_\ell^\nu(\widehat{\boldsymbol{k}})\sqrt{\frac{K_{\alpha'}}{K_\alpha}} \\
&\times \sum_L\sum_{L'}\sum_J \sqrt{2L+1}\langle LM_Ljm_j|JM\rangle\langle L'M_{L'}j'm_{j'}|JM\rangle e^{i(\sigma_L+\sigma_{L'})} \\
&\times S_{\beta\beta'}(K_{\beta'})Y_{L'}^{M_{L'}}(\widehat{\boldsymbol{R}}),
\end{aligned}$$ (3.42)

where

$$h(k) = \frac{4\pi}{k}\sum_\alpha(-i)^\ell e^{[\sigma_\ell(k)+\delta_{\ell j}(k)]}\sqrt{\frac{2}{\pi W_\alpha}}\int_{k_i-1}^{k_i} dk\, \mathrm{g}_i(k).$$

The triple-differential breakup cross sections can be obtained as follows [114]

$$\frac{d^3\sigma}{d\widehat{\boldsymbol{k}}d\widehat{\boldsymbol{R}}d\varepsilon} = \frac{\mu_{cv}\mu_{pt}^2 k}{(2\pi)^5\hbar^6}\frac{K_\alpha}{K_{\alpha_b}}\frac{1}{2J+1}\sum_{\nu m_j}\left|\mathcal{T}_{\nu\mu}^{m_j}(\boldsymbol{k}, \boldsymbol{K}_\beta)\right|^2.$$ (3.43)

Carrying out an integration over the solid angle $\widehat{\boldsymbol{k}}$, with the substitution of equation(3.42) into equation (3.43), leads to the following double-differential breakup cross section

$$\begin{aligned}
\frac{d^2\sigma}{d\widehat{\boldsymbol{R}}d\varepsilon} &= \int\frac{d^3\sigma}{d\widehat{\boldsymbol{k}}d\widehat{\boldsymbol{R}}d\varepsilon}d\widehat{\boldsymbol{k}} \\
&= \frac{\mu_{cv}K_\alpha}{4\pi^{\frac{5}{2}}\hbar^2 kK_{\alpha_b}^3}\frac{1}{2j+1}\sum_{\nu m_j\ell jm_j\nu'j'\mu}\langle\ell\nu s\mu|jm_j\rangle\langle\ell'\nu's\mu|j'm_{j'}\rangle \\
&\times \int d\widehat{\boldsymbol{k}}Y_\ell^{\nu\star}(\widehat{\boldsymbol{k}})Y_{\ell'}^{\nu'}(\widehat{\boldsymbol{k}})\bigg|\sum_{i'}h(k)\sqrt{\frac{K_{i'}}{K_i}}\sum_L\sum_{L'}\sum_J\sqrt{2L+1} \\
&\times \langle LM_Ljm_j|JM\rangle\langle L'M_L'j'm_j'|JM\rangle e^{i(\sigma_L+\sigma_{L'})}S_{ii'}^J(K_{i'})Y_{L'}^{M_{L'}}(\widehat{\boldsymbol{R}})\bigg|^2.
\end{aligned}$$ (3.44)

If one applies again the properties of Clebsh-Gordan as well as of spherical harmonics, the equation above reduces to

$$
\begin{aligned}
\frac{d^2\sigma}{d\widehat{\boldsymbol{R}}d\varepsilon} &= \frac{\mu_{cv}K_\alpha}{4\pi^{\frac{5}{2}}\hbar^2kK_{\alpha_b}^3}\frac{1}{2j+1}\sum_{\nu j}\left|\sum_{i'}h(k)\sqrt{\frac{K_{i'}}{K_i}}\sum_{LL'J}\sqrt{2L+1}\sum_{\ell'j'\nu'}\langle\ell\nu s\mu|jm_j\rangle\langle\ell'\nu's\mu|j'm_{j'}\rangle\right. \\
&\times \left.\langle LM_Ljm_j|JM\rangle\langle L'M_L'j'm_j'|JM\rangle e^{i(\sigma_L+\sigma_{L'})}S_{ii'}^J(K_{i'})Y_{L'}^{M_{L'}}(\widehat{\boldsymbol{R}})\right|^2.
\end{aligned}
\tag{3.45}
$$

The integration of the double-differential breakup cross sections over the excitation energy $d\varepsilon$, gives the following differential angular distribution breakup cross section

$$
\frac{d\sigma}{d\Omega} = \int d\varepsilon\frac{d^2\sigma}{d\Omega d\varepsilon},
\tag{3.46}
$$

($\Omega \equiv \widehat{\boldsymbol{R}}$) and the integration of the solid angle $d\Omega$, gives the following differential energy distribution breakup cross section

$$
\frac{d\sigma}{d\varepsilon} = \int d\Omega\frac{d^2\sigma}{d\Omega d\varepsilon}.
\tag{3.47}
$$

The integrated breakup cross section is obtained from equation (3.46) as follows

$$
\begin{aligned}
\sigma &= \int d\Omega\frac{d\sigma}{d\Omega} \\
&= 2\pi\int_0^\pi \sin\theta d\theta\frac{d\sigma}{d\Omega}.
\end{aligned}
\tag{3.48}
$$

Also, the integrated breakup cross section directly derived from the corresponding scattering matrix elements as follows [104]

$$
\begin{aligned}
\sigma &= \sum_J \sigma_J \\
\sigma_J &= \frac{\pi}{K_{\alpha_b}^2}\sum_\beta\sum_L\sum_{L'}\frac{2J+1}{2J_b+1}\left|S_{\beta\beta'}(K_{\beta'})\right|^2.
\end{aligned}
\tag{3.49}
$$

As for other breakup observables such total fusion cross section, it can be obtained from

the imaginary part of the coupling matrix elements (3.16)

$$W_{\alpha\alpha'}^{LL'J}(R) = \left\langle \mathscr{Y}_{\alpha}^{LJ}(\boldsymbol{r},\Omega_{\widehat{\boldsymbol{R}}})|W_{ct}(\boldsymbol{R}_{ct}) + W_{pt}(\boldsymbol{R}_{pt})|\mathscr{Y}_{\alpha'}^{L'J}(\boldsymbol{r},\Omega_{\widehat{\boldsymbol{R}}})\right\rangle,$$ (3.50)

as well as the whole breakup wave function. This means that the fusion cross section is the expectation value of the imaginary part with the breakup wave function, given by [102, 103]

$$
\begin{aligned}
\sigma_{\text{TF}} &= \sum_{J} \sigma_{\text{TF}}^{J} \\
\sigma_{\text{TF}}^{J} &= \frac{2\mu_{pt}}{\hbar^2 K_d}(2L+1)\sum_{\alpha\alpha'}\left\langle F_{\alpha}^{LJ}(R)\middle|W_{\alpha\alpha'}^{LL'J}(R)\middle|F_{\alpha'}^{L'J}(R)\right\rangle.
\end{aligned}
$$ (3.51)

In this chapter, we have discussed the dynamics of the three-body scattering states. Steps leading to the coupled differential equations have been highlighted. The resulting coupling matrix elements are derived in details, as well as the breakup cross sections. The next chapter outlines the various input parameters that are needed to solve two-body differential equation (2.15), and the coupled differential equations (3.13).

Chapter 4

Details of numerical calculations

As indicated in the introduction, the reaction that we are investigating in this dissertation is ^{11}Be + ^{208}Pb at various incident energies. In this chapter, we mainly discuss the numerical parameters that are useful in the numerical solution of the coupled differential equations (3.13) related to this reaction. These parameters are those related to the CDCC model space, the core-target and neutron-target optical potentials and to the internal structure of ^{11}Be projectile nucleus. Due to the relevance of the internal structure of the projectile in the breakup process, as already shown in chapter 3, we start by describing the internal structure of the ^{11}Be nucleus. The choice of this nucleus as a projectile in the present work is motivated in the introduction.

4.1 Description of the ^{11}Be projectile nucleus

As already indicated in the introduction, the ^{11}Be nucleus is a well established one-neutron halo nucleus [7,90,105,106], with a few-body structure, where it is formed by the ^{10}Be core nucleus and a halo neutron which is weakly-bound to the core nucleus (^{11}Be $\longrightarrow$ ^{10}Be$+n$), with an experimental ground-state binding energy of 0.504 ±0.006 MeV [109]. Its ground-state is an s-state, identified by the following quantum numbers $\ell_b = 0$, $s = \frac{1}{2}$ and $j_b = \frac{1}{2}^+$. Its first excited state ($1p_{\frac{1}{2}^-}$ state) is a bound-state, with a binding energy of 0.184 ±0.007 MeV. Its continuum contains a narrow resonance 1.274 ±0.018 MeV, in the continuum state $d_{\frac{5}{2}^+}$ [108]. For the sake of simplicity, in the present study, we considering an inert core nucleus, meaning that we do not take into account its internal structure during the breakup process. Therefore, we only consider the following ^{11}Be $\rightarrow \left| ^{10}\text{Be}(0^+) \otimes n(2s_{\frac{1}{2}^+}) \right\rangle$ ground state configuration.

4.1.1 Bound-state structure and wave function

The ground-state wave function is an important parameter in the breakup process. It is well-known that a lower breakup threshold corresponds to an extended ground-state wave function to the peripheral region. Due to the the peripheral nature of the breakup process, the extension of the wave function plays an important role in the breakup process. Also, one can obtain different ground-state properties such as the size of the system, once the ground-state wave function is known. To obtain the ground-state as well as the first excited bound-state wave functions, the two-body Schrödinger equation (2.15), was numerically solved with the boundary conditions (2.20). For the core-neutron potential we adopted the Woods-Saxon shape, given by equation (2.46), whose parameters listed in Table 4.1, where V_0^ℓ and $V_{\rm SO}$ are depths of the central and spin-orbit coupling terms,

Table 4.1: Numerical values of the ^{10}Be $+ n$ potential parameters (V_0^ℓ, R_0, a_0) and $(V_{\rm SO}, R_{\rm SO}, a_{\rm SO})$, taken from Ref. [64].

System	$V_0^{\ell=0}$	$V_0^{\ell>0}$	R_0	a_0	$V_{\rm SO}$	$R_{\rm SO}$	$a_{\rm SO}$
	(MeV)	(MeV)	(fm)	(fm)	(MeV $\cdot$ fm^2)	(fm)	(fm)
^{10}Be $+ n$	59.5	40.5	2.699	0.6	32.8	2.99	0.6

and $(R_0, a_0), (R_{\rm SO}, a_{\rm SO})$ are the corresponding radii and diffuseness. All these parameters were taken from Ref. [64]. The components $V_0^{nucl}(r)$ and $V_{\rm so}^{nucl}(r)$ of the nuclear potential $V_{cv}^{nucl}(r)$ are plotted in Table 4.1. As one would expect, this potential vanishes rapidly beyond $r \geq R_{\rm x}$ (x $\equiv 0, {\rm SO}$). The ground-state and first excited bound-state wave functions
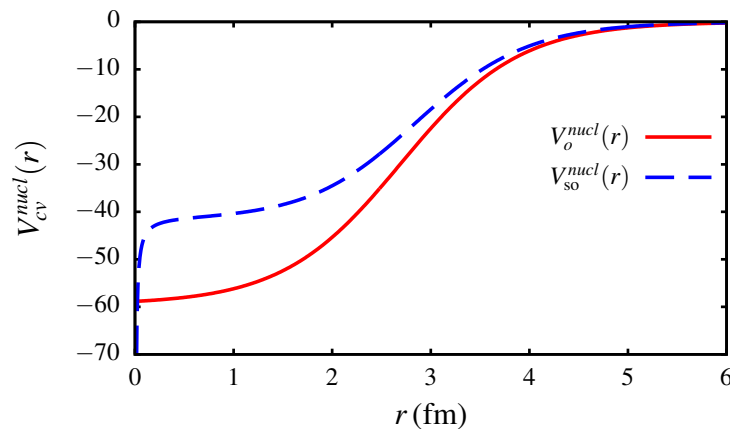

Figure 4.1: Core-neutron nuclear potential $V_{cv}^{nucl}(r)$ of the ^{10}Be$+n$ system. The spin-orbit coupling term $V_{\rm so}^{nucl}(r)$ is calculated in the $p_{1/2}$-state.
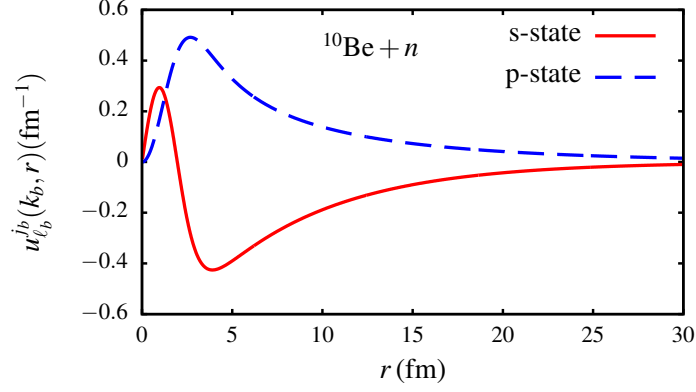
Figure 4.2: Wave functions of the ground ($s_{1/2}$-state) and first excited bound-state ($p_{1/2}$-state) for the $^{10}\mathrm{Be} + n$ system.

are depicted in Figure 4.2. To better check the extension of the wave function to the peripheral region we consider the root-mean-square radius, defined as

$$\sqrt{\langle r^2 \rangle} = \frac{1}{\sqrt{2A}} \left(\int_0^\infty |u_{k_b \ell_b}^{j_b}(r)|^2 r^2 dr \right)^{1/2}, \tag{4.1}$$

where A is the atomic mass number. For the ground-state, we obtained $\sqrt{\langle r^2 \rangle} = 5.77\,\mathrm{fm}$, which is similar to $\sqrt{\langle r^2 \rangle} = 5.77 \pm 0.16\,\mathrm{fm}$ obtained from an experimental study of this system [16]. Comparing this value to the radius of the $^{10}\mathrm{Be}$ core nucleus, which is $R_{core} = 2.36\,\mathrm{fm}$ [122], we see that core nucleus radius represents about 40% of the system such that the remainder accounts for the halo state.

4.1.2 Continuum structure and dipole electric response function

The continuum structure of a weakly-bound system plays an important role in this process. Resonant states have been reported to influence different reaction observables such as elastic scattering, breakup cross sections, fusion, etc., as exemplified for example by Refs. [112, 113]. In Figure 4.3, we plot the phase shifts (in degrees), in terms of the excitation energy ε (in MeV). The continuum wave functions were calculated with the same core-neutron potential parameters given Table 4.1. That figure indicates three resonances in s-state and d-states. However, only the $\mathrm{d}_{5/2+}$ narrow resonance is know experimentally [108]. According to the first-order approximation theory [117–120], the Coulomb breakup cross section cross section is directly proportional to the structure of the projectile nucleus through its dipole electric response function. To explicitly show
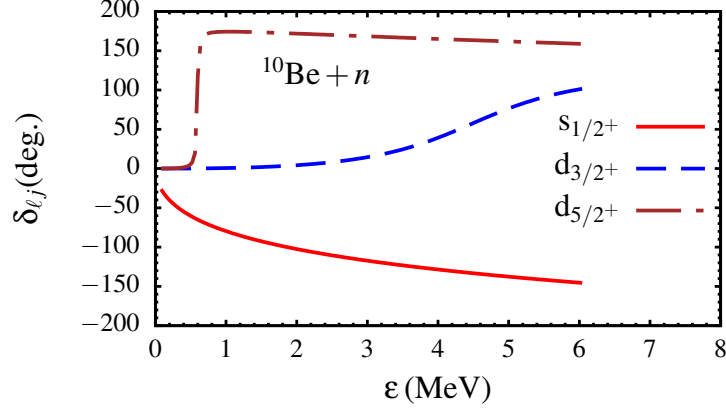
Figure 4.3: Phase shifts in s and d partial waves, shown as functions of the excitation energy for the $^{10}\text{Be} + n$ system.

this dependence, notice that equation (3.30) contains the factor $\langle \phi_{\alpha_b}^{m_{j_b}}(\boldsymbol{r}) | \mathcal{M}_\lambda^\epsilon(\boldsymbol{r}) | \phi_\gamma^{m_j}(\boldsymbol{r}) \rangle$, with the electric operator $\mathcal{M}_\lambda^\epsilon(\boldsymbol{r})$, given by equation (3.28), and the bound-state $\phi_{\alpha_b}^{m_{j_b}}(\boldsymbol{r})$ and scattering states $\phi_\gamma^{m_j}(\boldsymbol{r})$ wave functions are given by equation (2.14). The dipole electric response function of the transition from the ground-state to the continuum can be obtained in terms of this factor as follows is given by [9]

$$\frac{dB(E1)}{d\varepsilon} = \frac{\mu_{cv}}{\hbar^2 k} \sum_j (2j+1) \left| \langle \phi_{\alpha_b}^{j_b}(\boldsymbol{r}) | \mathcal{M}_\lambda^\epsilon(\boldsymbol{r}) | \phi_\gamma^j(\boldsymbol{r}) \rangle \right|^2. \tag{4.2}$$

Expanding this factor as in section 3.5, we obtain

$$\begin{aligned}
\frac{dB(E1)}{d\varepsilon} &= \frac{\mu_{cv}}{\hbar^2 k} \sum_j (2j+1) \left| eZ_\lambda (-1)^{\ell_b + \ell + j + s + \lambda} \begin{pmatrix} \ell_b & \lambda & \ell \\ 0 & 0 & 0 \end{pmatrix} \right. \\
&\quad \times \left. \begin{Bmatrix} s & \ell_b & j_b \\ \lambda & j' & \ell \end{Bmatrix} \int_0^\infty u_{\ell_b}^{j_b}(k_b, r) r^\lambda u_\ell^j(k, r) dr \right|^2,
\end{aligned} \tag{4.3}$$

where Z_λ is the effective charge, given by equation (3.29), $u_{\ell_b}^{j_b}(k_b, r)$ and $u_\ell^j(k, r)$ are the ground-state and continuum radial wave functions, normalized according to equations (2.20) and (2.29). The electric response function calculated using the computer code RADCAP [123], is plotted in figure 4.4 as function of the excitation energy ε. As one can see, the response function has a peak around the binding energy, which is a characteristic of weakly-bound systems. One also sees that the relevant contribution to the response
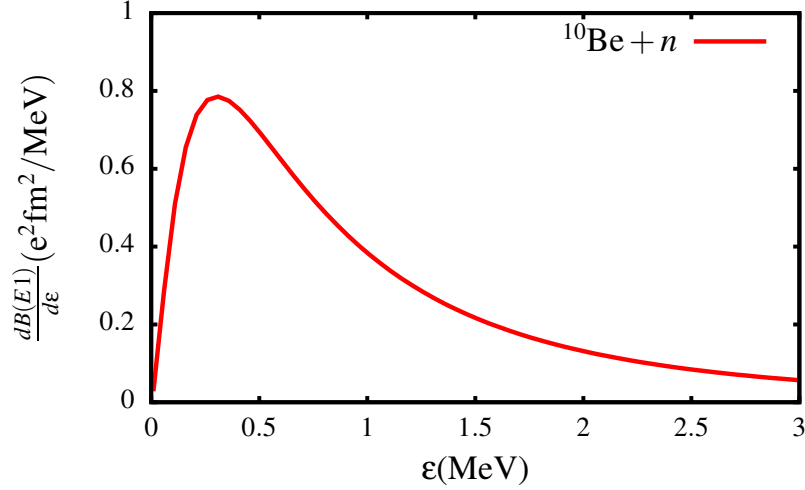
Figure 4.4: Plot of the dipole electric response function of the $^{10}\text{Be} + n$ system obtained for the transition from the ground-state to p-state.

function is located at $\varepsilon \leq 1.0 \,\text{MeV}$. Following Refs. [117, 120], we can show that the dipole response function is related to the Coulomb breakup cross section through the following equation

$$\frac{d\sigma_C^{E1}}{d\varepsilon} = \frac{32\pi^2}{9}\left(\frac{Z_t e}{\hbar v}\right)^2 z_m \mathcal{K}_0(z_m)\mathcal{K}_1(z_m)\frac{dB(E1)}{d\varepsilon}, \qquad (4.4)$$

where $Z_t e$, is the target nucleus charge, v, velocity of the the projectile, given by $v = \sqrt{2E/\mu_{pt}}$ (E being the incident energy), and

$$z_{min} = \frac{\varepsilon - \varepsilon_0}{\hbar v}\left[\frac{Z_p Z_t e^2}{2E \tan(\frac{\theta_c}{2})}\right], \qquad (4.5)$$

with θ_c the cut-off angle, and $\mathcal{K}_0$ and $\mathcal{K}_1$ are modified Bessel functions of the second kind of order 0 and 1 [100]. As an illustration, we use equation (4.5) to study the first-order Coulomb breakup cross section for the $^{11}\text{Be} + {}^{208}\text{Pb}$ reaction at a laboratory incident energy $E_{lab} = 68 \,\text{MeV}/A$. With $\mu_{pt} = 9732 \,\text{MeV/c}^2$, the velocity is $v \simeq 0.277c$, where $c = 3 \times 10^8 \,\text{m/s}$, is the speed of light in vacuum. The calculated Coulomb breakup cross section as function of the energy energy ε is plotted Figure 4.5, for $\theta_c = 6°$ and $\theta_c = 4.5°$. One can see that the theoretical calculations are in good agreement with the experimental data that were taken from Ref. [16, 110].
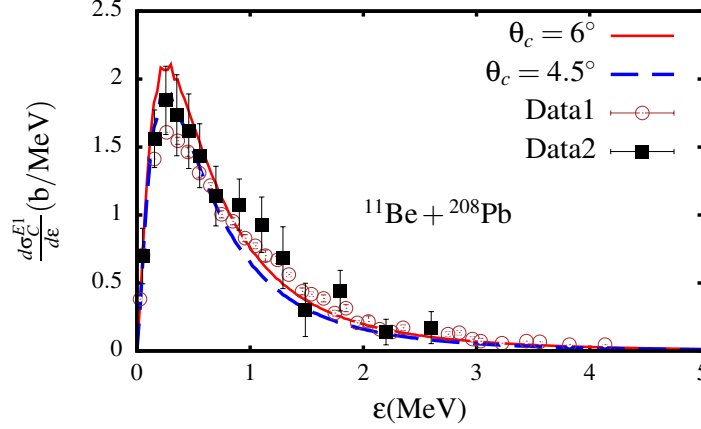
Figure 4.5: Coulomb breakup cross sections, plotted as functions of the projectile excitation energy ε, obtained using Eq.(4.5), in the breakup of ^{11}Be projectile on the ^{208}Pb target at a laboratory incident energy $E_{lab} = 68$ MeV/A. The two sets of experimental data points were obtained in Ref. [16], and Ref. [110].

4.2   Core-target and neutron-target potentials

In order to solve the coupled differential equations (3.13), we also need the the numerical parameters of core-target and neutron-target optical potentials. We are not interested in the event where possibly all three particles are interacting simultaneously, leading to a three-body interaction. Such interaction is not included in our numerical calculations. The nuclear part of the core-target optical potential is given by the Woods-Saxon form factor similar to that in equation (2.47)

$$
\begin{aligned}
U_{ct}(R_{ct}) &= V_{ct}(R_{ct}) + iW_{ct}(R_{ct}) \\
&= \frac{V_0}{\left[1 + \exp(\frac{R_{ct} - R_0}{a_0})\right]} + \frac{iW_V}{\left[1 + \exp(\frac{R_{ct} - R_w}{a_w})\right]},
\end{aligned} \tag{4.6}
$$

where V_0 is the depth of the real part, and W_V, the depth of the imaginary parts, and R_x, a_x [$x \equiv (0, W)$] the corresponding radii and diffuseness. The core-target Coulomb potential also similar to equation (2.48), is

$$
V_{ct}^{coul}(R_{ct}) = \begin{cases} \dfrac{Z_c Z_t e^2}{R_C}\left(\dfrac{3}{2} - \dfrac{R_{ct}^2}{2R_C^2}\right) & R_{ct} \leq R_C, \\[4mm] \\ \dfrac{Z_c Z_t e^2}{R_{ct}} & R_{ct} > R_C, \end{cases} \tag{4.7}
$$

Table 4.2: Numerical parameters (V_0, R_0, a_0), (W_V, R_W, a_W), (W_D, R_D, a_D) and (V_{SO}, R_{SO}, a_{SO}), core-target and neutron-target optical potentials. For the neutron-target surface and spin-orbit terms, these parameters are $W_D = -0.908$MeV, $R_D = 7.397$ MeV, $a_D = 0.510$ MeV, $W_{SO} = 3.654$ MeV $\cdot$ fm^2, $R_{SO} = 6.376$ fm, and $W_{SO} = 0.590$ fm. The core-target potential parameters were obtained from the global parametrization of Akyuz-Winther [116], whereas for the neutron-target potential, the global parametrization of Koning [111], was used.

| | V_0 | R_0 | a_0 | W_V | R_W | a_W |
	(MeV)	(fm)	(fm)	(MeV)	(fm)	(fm)
^{10}Be + ^{208}Pb	-51.978	9.515	0.64	-12.994	9.515	0.64
$n + ^{208}$Pb	-35.684	7.32	0.647	-3.216	7.32	0.647

The neutron-target potential U_{vt} is given by

$$U_{vt}(R_{vt}) = V_{vt}(R_{vt}) + V_{vt,\text{SO}}(R_{vt}) + i[W_{vt}(R_{vt}) + W_{vt,\text{D}}(R_{vt})], \tag{4.8}$$

$V_{vt}(R_{vt})$ is the central term, $V_{vt,\text{SO}}(R_{vt})$, the spin orbital term (both terms represent the real part of the potential), $W_{vt}(R_{vt})$ and $W_{vt,\text{D}}(R_{vt})$ represent the volume and surface terms of the imaginary part. All these potential terms are given by the Woods-Saxon form factor, meaning that

$$
\begin{aligned}
V_{vt}(R_{vt}) &= V_0 f(R_{vt}, R_0, a_0), \\
W_{vt}(R_{vt}) &= W_V f(R_{vt}, R_W, a_W, \\
W_{vt,\text{D}}(R_{vt}) &= -4a_\text{D} W_\text{D} \frac{d}{dR_{vt}} f(R_{vt}, R_\text{D}, a_\text{D}), \\
V_{vt,\text{SO}}(R_{vt}) &= V_\text{SO} (\boldsymbol{L.s}) \left(\frac{\hbar}{m_\pi c}\right)^2 \frac{1}{R_{vt}} \frac{d}{dR_{vt}} f(R_{vt}, R_\text{SO}, a_\text{SO}),
\end{aligned}
\tag{4.9}
$$

$$f(R_{vt}, R_x, a_x) = \frac{1}{\left[1 + \exp\left(\frac{R_{vt} - R_x}{a_x}\right)\right]}. \tag{4.10}$$

The numerical values parameters core-target and neutron-target potential parameters are displayed in Table 4.2. For the core-target optical potential, the different parameters were obtained from the global parametrization of Akyuz-Winther [116], whereas neutron-

target potential parameters were obtained from the global parametrization of Koning [111]. Apart from the off-diagonal nuclear potential, we also include a monopole nuclear interaction in the elastic scattering channel with both real and imaginary parts $[U_{bb}(R) = V_{bb}(R) + iW_{bb}(R)]$. This potential is obtained by folding the core-target and neutron-target potentials with the density of the ground-state projectile wave function. That is

$$
\begin{aligned}
V_{bb}(R) &= \int d^3r |\phi_b^{m_j}(\boldsymbol{r})|^2 [V_{ct}(R_{ct}) + V_{nt}(R_{nt})] \\
W_{bb}(R) &= \int d^3r |\phi_b^{m_j}(\boldsymbol{r})|^2 [V_{ct}(W_{ct}) + W_{nt}(R_{nt})].
\end{aligned}
\tag{4.11}
$$

This potential, as such takes into account the halo nature of the projectile nucleus. Owing to the long tail of the halo ground-state wave function, the nuclear potential thus obtained has a long-range compared to a phenomenological short-range nuclear potential, which assumes the projectile to be a one-body system. In Ref. [4], a comparison of both potentials was performed and it was the importance of structure in the ground state was elucidated.

4.3   CDCC numerical parameters

In order to numerically solve the coupled differential equations (3.13), another set of numerical parameters is needed. These parameters are to be optimized in order to achieve convergence. The numerical values of these parameters are given in Table 4.3, where

- ℓ_{max}: is the maximum value of the core-nucleon orbital angular momentum.
- λ_{max}: is the maximum value of the multipole order in the potential multi pole expansion.

- ε_{max}: is the maximum value of the bin energy.
- r_{max}: is the maximum value of the matching matching radius for bin integration.
- Δr: is the integration step size in the discretization of the maximum matching radius $r_{\max}$.
- L_{max}: is the maximum value of the orbital angular momentum associated with projectile-target relative center-of-mass motion.

- R_{max}: is the maximum value of the matching radius in the numerical integration of the coupled differential equations.

- ΔR: is the integration step size in the discretization of the maximum matching radius with R_{max}.

Table 4.3: Optimal numerical parameters ℓ_{max},λ_{max},ε_{max}, r_{max}, R_{max}, L_{max}, Δr and ΔR adopted in the numerical solution of the coupled equations solutions.

ℓ_{max}	λ_{max}	ε_{max}	r_{max}	Δr	L_{max}	R_{max}	ΔR
$(\hbar)$	-	(MeV)	(fm)	(fm)	$(\hbar)$	(fm)	(fm)
6	6	10	120	0.1	10000	1000	0.05

Having discussed the various input parameters, the next chapter focuses on the results obtained in the ^{11}Be+^{208}Pb breakup reaction at various sub-barrier incident energies. The numerical calculations were carried out using FRESCO computer codes [114, 115].

Chapter 5

Results and Discussions

In this chapter, we study the breakup of the ^{11}Be neutron-halo nucleus on ^{208}Pb target, at below and around the Coulomb barrier incident energies. As already mentioned in the introduction, the main objective of this dissertation is to study dynamics of a neutron-halo projectile nucleus considering incident energies below and around the Coulomb barrier. Interested in investigating whether the conclusions drawn for the ^{8}B proton-halo system in Refs. [21,22,95] in the same energy region can be extended to its neutron-halo counterpart. In particular, we will verify whether at such incident energies, the breakup cross section remains the main reaction channel as it has been shown in the case of ^{8}B system. We consider the ^{11}Be$+^{208}$Pb in the incident energy range $0.5 \leq E_{cm}/V_{\mathrm{B}} \leq 1.2$, with V_{B}, being the Coulomb barrier height, which was calculated with the São Paulo potential [121].

5.1 Convergence analysis of the breakup cross sections

Before we dive into the analysis of the results, let us first discuss the convergence of the numerical calculations, namely the breakup cross section. In Section 4.3, we have enumerated the a number of numerical parameters that are adopted in the numerical solution of the coupled differential equations (3.13). Although the convergence was checked with respect to other numerical parameters, and incident energies, we only discuss the convergence of the breakup cross section as function of the centre-of-mass angle θ, in terms of ε_{max}, ℓ_{max}, λ_{max}, and r_{max}, at $E_{cm}/V_{\mathrm{B}} = 0.9$, $E_{cm}/V_{\mathrm{B}} = 1.0$ and $E_{cm}/V_{\mathrm{B}} = 1.2$ incident energies, where $V_{\mathrm{B}} = 38.87\,\mathrm{MeV}$. In the left panel of figure 5.1 [panels (a')] the convergence of the breakup cross section is shown in terms of the maximum bin energy ε_{max}. Inspecting that figure, we notice that for $E_{cm}/V_{\mathrm{B}} = 0.9$, the convergence is achieved for $\varepsilon_{max} = 6\,\mathrm{MeV}$, since the curve corresponding to $\varepsilon_{max} = 6\,\mathrm{MeV}$, and the
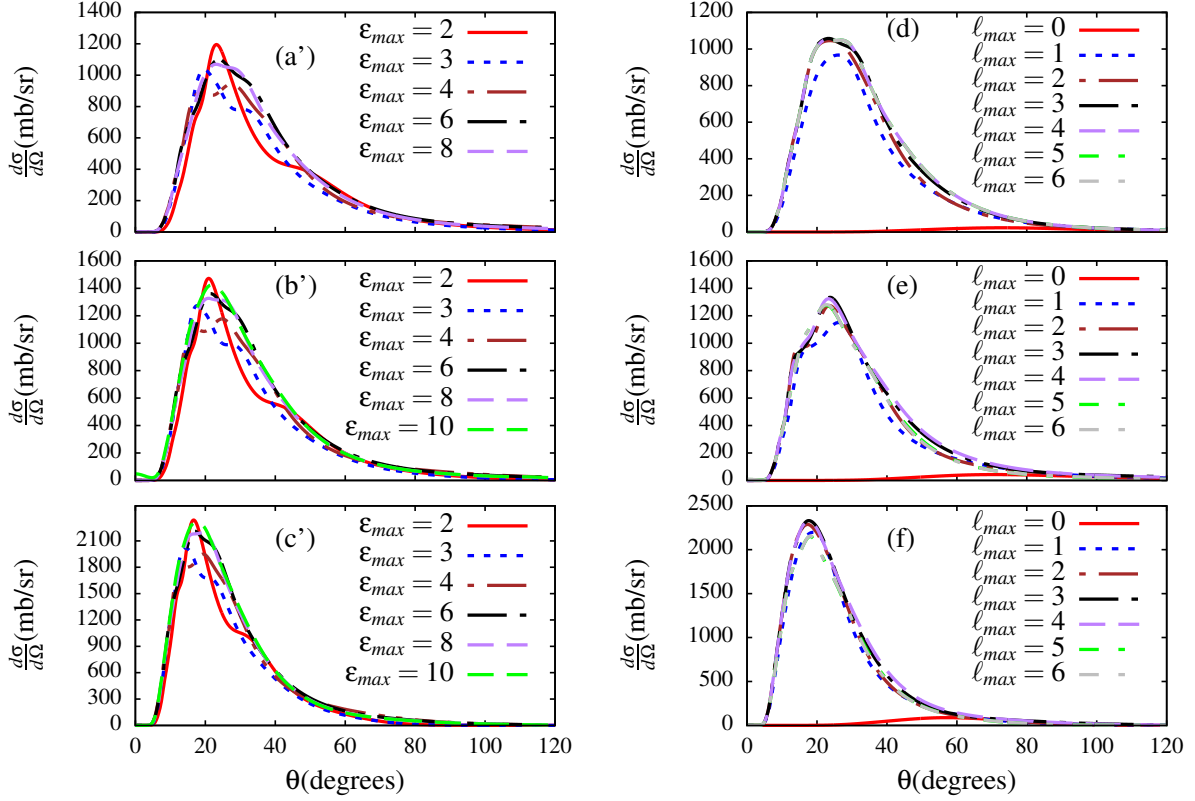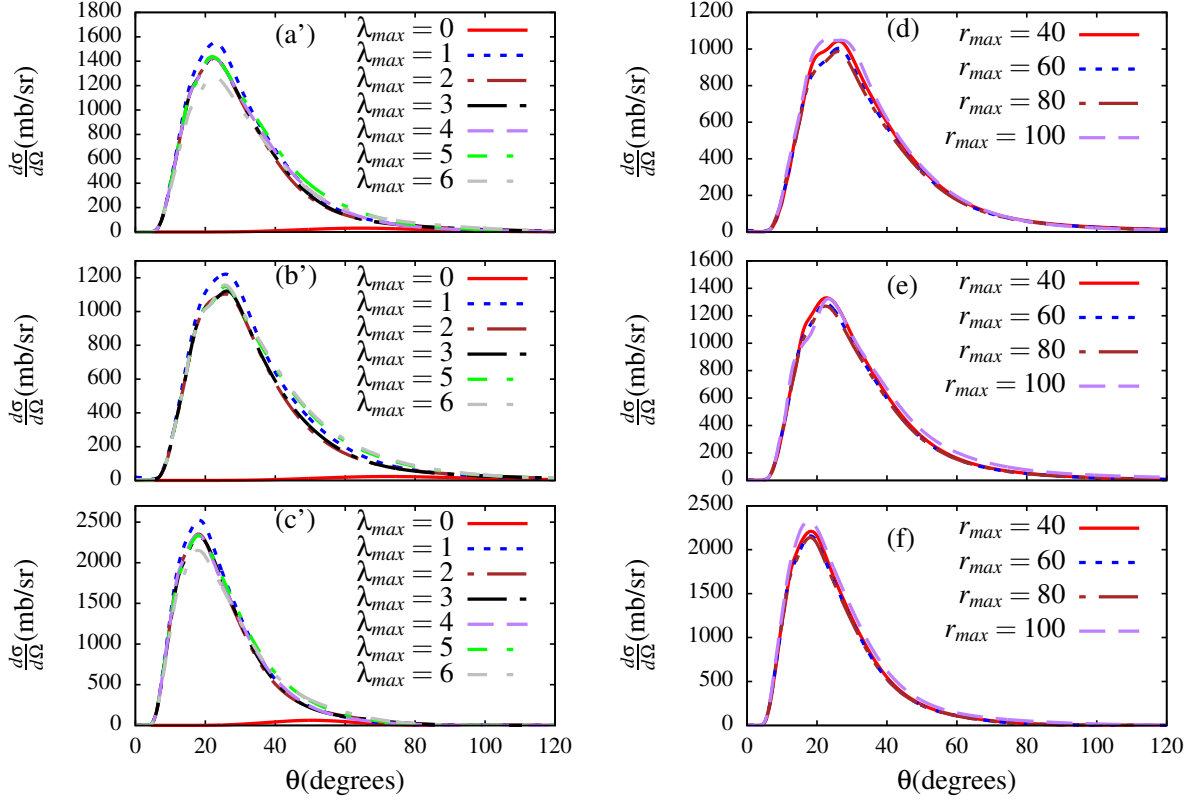

(a) Convergence in terms of ε_{max} (b) Convergence in terms of ℓ_{max}

Figure 5.1: Convergence of the angular distributions differential breakup cross section as function of the Laboratory angle θ in terms of the maximum projectile excitation energy ε_{max} and the maximum orbital core-neutron angular momentum ℓ_{max}. The top panel corresponds to $E_{cm}/V_B =0.9$, the middle panel corresponds to $E_{cm}/V_B =1.0$, and lower panel corresponds to $E_{cm}/V_B =1.2$, where E_{cm} is the projectile incident energy in the projectile-target center of mass, and V_B is the projectile-target Coulomb barrier height.

one corresponding to $\varepsilon_{max} = 8\,\text{MeV}$ are hardly distinguishable. In other words we can say that ,$\dfrac{d\sigma}{d\Omega}(\varepsilon_{max} = 6\,\text{MeV}) - \dfrac{d\sigma}{d\Omega}(\varepsilon_{max} = 8\,\text{MeV}) \to 0$. Although for $E_{cm}/V_B = 1.0$ and $E_{cm}/V_B = 1.2$ incident energies [panels (b') and (c')] the convergence appears to be achieved for $\varepsilon_{max} = 6\,\text{MeV}$, we noted that maximum bin energies up to $\varepsilon_{max} = 10\,\text{MeV}$ were needed to guarantee a satisfactory convergence. Another striking aspect in that figure is the fact that the breakup cross section is dominated by lower bin energies. One observes that $\varepsilon_{max} = 2\,\text{MeV}$ accounts for the main contribution to the breakup cross section in all three cases, and corresponds to narrow breakup cross sections around the peak (around $20°$). This is in accordance with the breakup cross sections of weakly-bound systems, which are known to peak around the breakup threshold (for example, see Fig.4.5 where the peak of the breakup cross section is located around the breakup threshold ε_b).The

Figure 5.2: Convergence of the angular distributions differential breakup cross section as function of the Laboratory angle θ in terms of the maximum multi-pole expansion λ_{max}, and the maximum core-neutron radial coordinate r_{max}. The top panel corresponds to $E_{cm}/V_{\rm B} = 0.9$, the middle panel corresponds to $E_{cm}/V_{\rm B} = 1.0$, and lower panel corresponds to $E_{cm}/V_{\rm B} = 1.2$, where E_{cm} is the projectile incident energy in the projectile-target center of mass, and $V_{\rm B}$ is the projectile-target Coulomb barrier height.

convergence of the breakup cross section as function of the maximum core-neutron orbital angular momentum ℓ_{max} is displayed in panel (b) of Figure 5.1. Observing that figure, one sees that the convergence is achieved for $\ell_{max} = 3$, since higher partial waves do not seem to have any meaningful contribution to the cross section. In panels (d), (e) and (f), we notice that the contribution of the s-wave ($\ell_{max} = 0$), is quite small. We notice that p-waves ($\ell_{max} = 1$) account for the largest contribution to the breakup cross section. Also, although higher partial waves seem to be important in the convergence of the calculations, their observed overall contribution to the breakup cross section is rather small compare to the contribution of p-waves. A larger contribution to the breakup cross section by p-waves, is a signature of breakup reactions involving weakly-bound systems. Panel (a) of figure 5.2, displays the convergence of the breakup cross section in terms of

the maximum multi-pole order in the potential multi-pole expansion λ_{max}. One notices that in all three cases, the monopole order $\lambda_{max} = 0$, represents a small contribution, and dipole order $\lambda_{max} = 1$, accounts for the largest contribution, as expected. This in fact the essence of the first-order approximation theory. This larger contribution can be explained by the fact dipole transition favours p-waves (see details for example in Ref. [97]). A careful observation of figure 5.2 (a'), shows that higher multi-pole orders ($\lambda_{max} \geq 2$) appear to reduce the breakup cross section. This can be seen as an effect of the higher order interference effect, which seems to be destructive in this case (again see Ref. [97], for details).Panel (b) of figure 5.2, displays the convergence of the breakup cross section as function of the maximum core-neutron internal radial coordinate r_{max}, or the maximum matching radius for bin integration for various values $r_{max} = 40$ to $r_{max} = 100$. We notice in all panels that the convergence of the results is already achieved convergence for $r_{max} = 40$, which implies that there is no compelling need to consider larger values of r_{max}, which would unnecessarily increase the computing burden. This implies that for $r_{max} = 40\,\text{fm}$, the orthogonal of the bin wave functions is already guaranteed. We have also checked the convergence of the fusion cross section against the various parameters, although the details are not presented here.

5.2   Comparison with experimental data

In order to further test the stability of our numerical calculations, we compare the angular-distributions breakup cross section with the experimental data. Because we are not aware of any measurement of the $^{11}\text{Be}+^{208}\text{Pb}$ reaction at the incident energies we are considering, we performed numerical calculations considering an incident energy of $E_{lab} = 140\,\text{MeV}$, for which there are experimental data [107]. The numerical calculations are compared with the experimental in figure 5.3, where a satisfactory agreement is observed. It is clear from this figure that the elastic breakup alone provides a better fit of the experimental data, such that there is no need of adding a contribution from the inelastic breakup component, which as apparent is not that relevant in fitting the data. The observed agreement between the numerical calculations and the experimental data is quite interesting because it is indicated in Ref. [107] (see also Ref. [7] and Ref. [98], among others) that to obtain
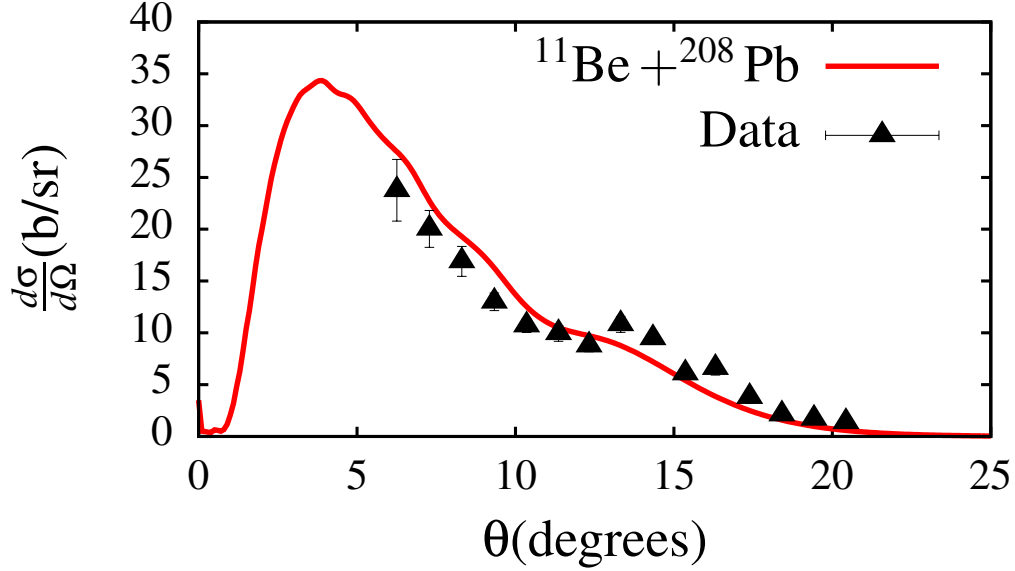
Figure 5.3: Angular distributions differential breakup cross section as a function of angle θ, compared with the experimental data, taken from Ref. [107]

a better fit of the experimental data one needs to add a contribution from the inelastic breakup cross section, indicating the relative significant of the latter, which is not reflected in the present case.

5.3 Breakup cross section versus total fusion cross section

Having discussed the convergence of the numerical calculations, we dedicate this section to the comparison of the breakup and total fusion cross section. Figure 5.4, shows the breakup and total fusion cross sections, plotted in terms of the ratio $E_{cm}/V_{\mathrm{B}} \in [0.5, 1.2]$, obtained with the inclusion of all various couplings in the couplings matrix elements "All coupl.", i.e., couplings to and from the ground-state as well as couplings among continuum states (continuum-continuum couplings). Inspecting that figure, one observes that at sub-barrier energies $(E_{cm}/V_{\mathrm{B}} \leq 1)$, the breakup cross section is quite dominant over the total fusion cross section. One sees that the transition occurs around the Coulomb barrier where the total fusion cross section prevails. Therefore, one infers that even for a weakly-bound neutron-halo projectile, the breakup channel remains the dominant reaction channel at sub-barrier incident energies. Therefore, it follows that even for a neutron-halo projectile
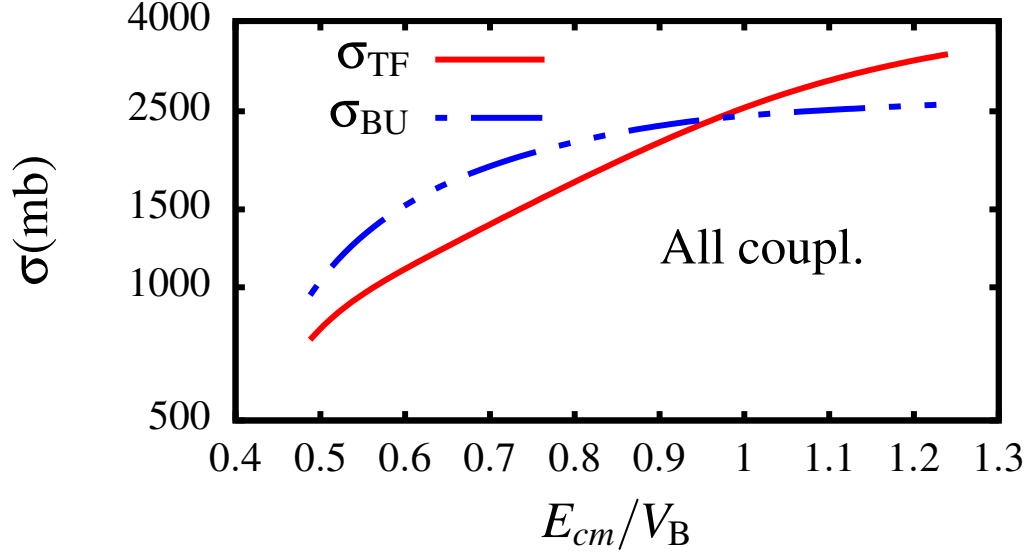
Figure 5.4: Breakup and total fusion cross sections plotted in terms of the incident energy scaled by the Coulomb barrier height V_{B}, and obtained with the inclusion of all the different coupled the coupling matrix elements.

such as ^{11}Be, the breakup cross section remains more dominant over the fusion cross section at sub-barrier energies, implying that the breakup channel is the most dominant reaction channel in this energy region. We can therefore conclude that the conclusions reported in Refs. [21, 22, 95] are as well extended to a neutron-halo projectile. This similarity highlights the fact that the Coulomb barrier in the core-proton system is not responsible for a dominant breakup cross section over the total fusion cross section at sub-barrier incident energies. That amounts to saying that, the static effect related to the tail of the projectile ground-state wave function is not the main factor that contributes to this phenomenon. As argued in Ref. [22], this leaves the dynamical effect, due to the projectile-target interaction to be one of the main factors that are responsible for a dominant breakup cross section over the total fusion cross section in this incident energy region.

5.3.1 Effect of the continuum-continuum couplings

In order to gain more insight into the observed dominance of the breakup cross section over the total fusion cross section at incident energies below the Coulomb barrier as observed in figure 5.4, we study the effect of the continuum-continuum couplings. As already pointed out in the introduction, continuum-continuum couplings (ccc) have been found
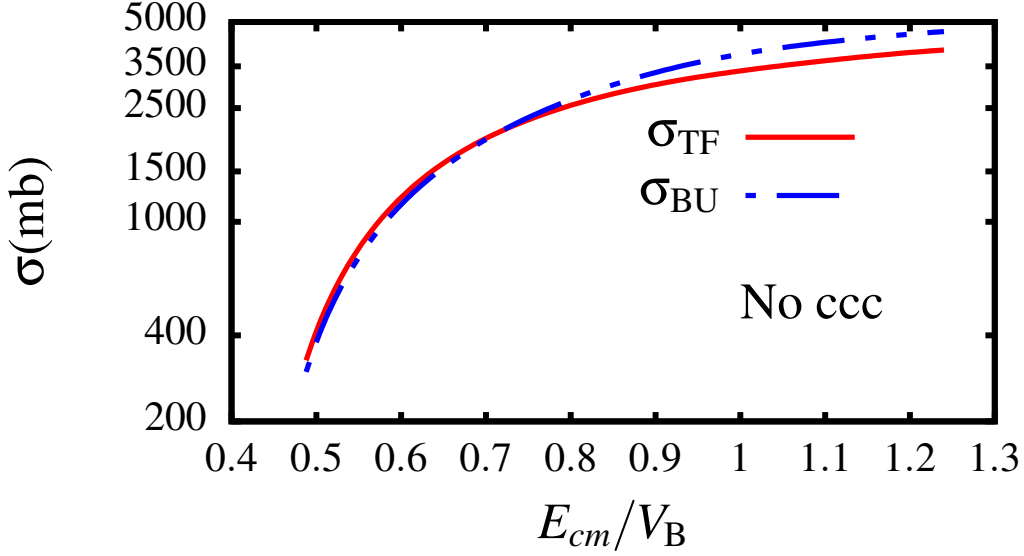
Figure 5.5: Breakup and total fusion cross sections plotted in terms of the incident energy scaled by the Coulomb barrier height V_{B}, and obtained with the exclusion of the continuum-continuum couplings from the coupling matrix elements ("No ccc").

to exhibit an important effect in the breakup of weakly-bound systems, and in fact, they are a signature of breakup reactions induced by weakly-bound systems. The relevance of these couplings have been mainly investigated for incident energies above the Coulomb barrier, where they are observed to strongly suppress the breakup cross section by orders of magnitude. Notice that with the inclusion of all the different couplings in the coupling matrix elements, they contains two radial integrals, namely $I_{\alpha_b\alpha}(R)$ and $I_{\alpha\alpha'}(R)$. As indicated in Chapter 3, the former represents couplings to and from the ground-state, and the latter represents continuum-continuum couplings, and it is given by equation (3.26). The most relevant information about couplings among different states of the projectile nucleus is contained in these radial integrals. When the continuum-continuum couplings are excluded $[I_{\alpha\alpha'}(R) = 0]$, the coupling matrix elements contain only the radial integral $I_{\alpha_b\alpha}(R)$. In that case, the CDCC method is reduced to standard one-step methods such as distorted wave Born approximation (DWBA). As we already mentioned in the introduction, the inclusion of $I_{\alpha\alpha'}(R)$ by the CDCC formalism, make it the most popular methods to probe the breakup dynamics of weakly-bound systems. In figure 5.5, we compare the total fusion and breakup cross sections obtained when the continuum-continuum couplings are removed from the couplings matrix elements ("No ccc"), meaning that $I_{\alpha\alpha'}(R) = 0$, leaving a single transition to and from the projectile bound-state, i.e., $I_{\alpha_b\alpha}(R) \neq 0$. In-

specting that figure, one registers a significant departure from figure 5.4, in the sense that at sub-barrier energies ($E_{cm}/V_{\mathrm{B}} \leq 0.8$), both breakup and total fusion cross sections are almost similar, with the two curves being hardly distinguishable. Above the Coulomb barrier, the breakup cross becomes dominant. Comparing figure 5.4 and figure 5.5, the continuum-continuum couplings appear to be responsible for the quantitative importance of the breakup cross section over the fusion cross section at sub-barrier incident energies, as also reported in Ref. [22]. For a better assessment of the effect on the breakup and total fusion cross section of the continuum-continuum couplings, we plot in figure 5.6 and figure 5.7, the breakup and fusion cross sections, respectively in the presence and absence of the continuum-continuum couplings. Starting with figure 5.6, we note that at

Figure 5.6: Integrated breakup cross sections plotted as functions of the incident energy scaled by the Coulomb barrier height V_{B}, and obtained with the inclusion of all the different couplings in the coupling matrix elements "All coupl." and with the exclusion of the continuum-continuum couplings from the couplings matrix elements "No ccc".

deep sub-barrier energies ($E_{cm}/V_{\mathrm{B}} \leq 0.7$), the continuum-continuum couplings serve to enhance the breakup cross section, as the breakup cross section in the presence of these couplings is larger than the breakup cross section in the absence of these couplings. A similar trend is reported in Ref. [113], for the breakup of the weakly-bound cluster system ^{6}Li on the same target nucleus. At larger incident energies ($E_{cm}/V_{\mathrm{B}} > 0.7$), the continuum-continuum couplings account for the suppression of the breakup cross section since in that case the breakup cross section obtained when the continuum-continuum couplings are removed is larger than the breakup cross section obtained when these couplings are
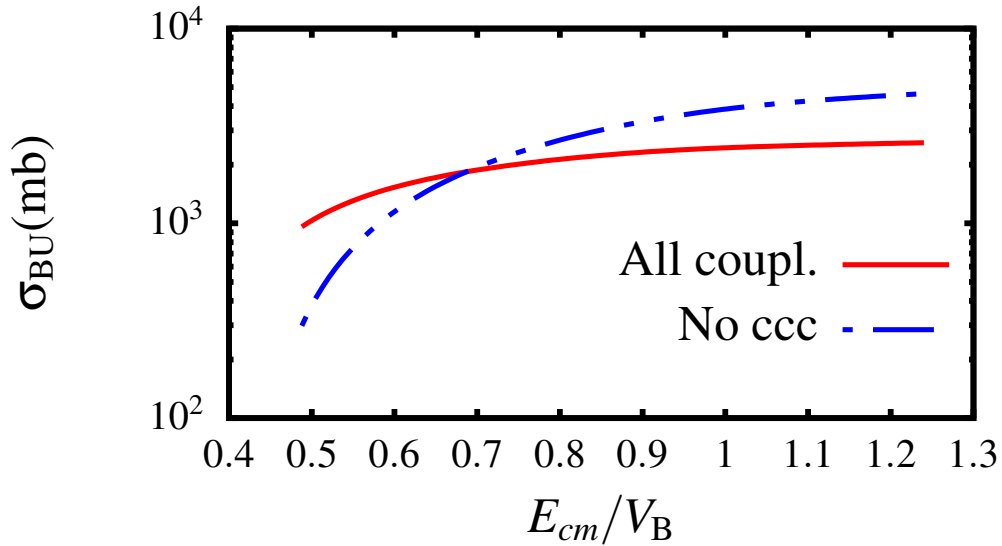
Figure 5.7: Total Fusion cross sections plotted as functions of the incident energy scaled by the Coulomb barrier height V_B, and obtained with the inclusion of all the different couplings in the coupling matrix elements "All coupl." and with the exclusion of the continuum-continuum couplings from the couplings matrix elements "No ccc".

included in the coupling matrix elements. In figure 5.7, we observe a similar trend where the fusion cross section is also enhanced by the continuum-continuum couplings at deep sub-barrier energies ($E_{cm}/V_B \leq 0.6$), and it is suppressed at higher incident energies. We already know that the breakup channel enhances fusion at sub-barrier energies (see for example Ref. [22]). To better visualize the enhancement and suppression of the breakup
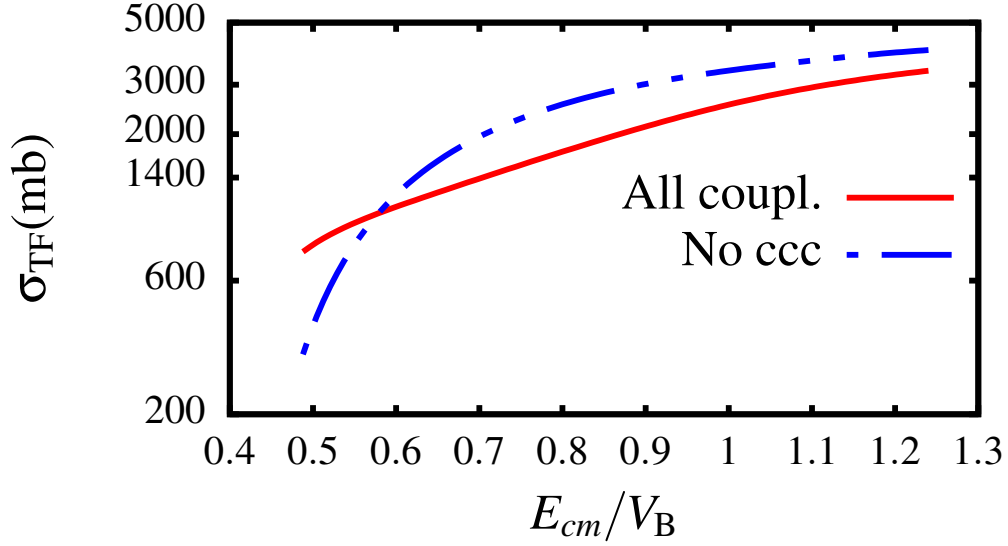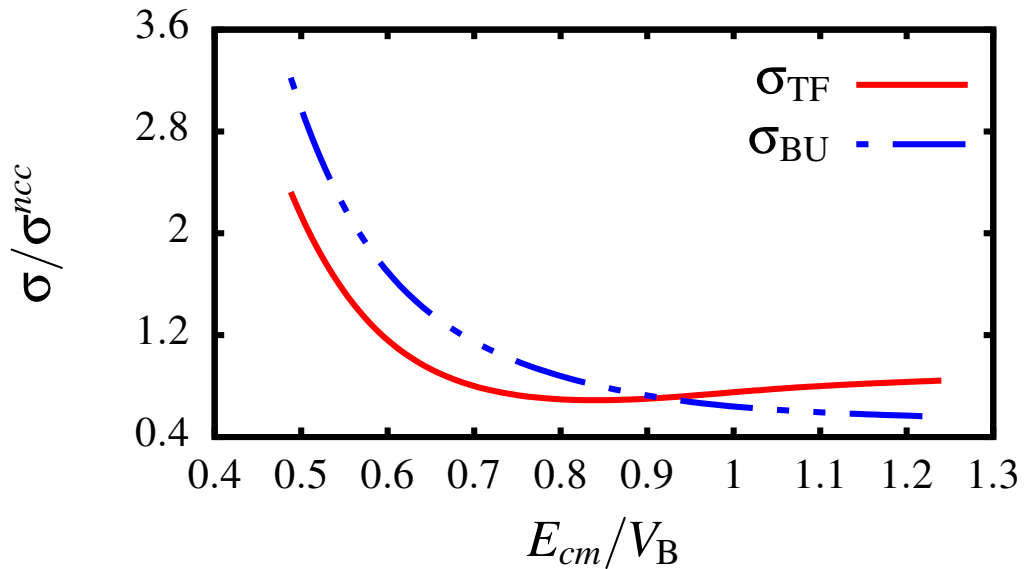

Figure 5.8: Breakup over fusion cross section plotted as functions of the incident energy scaled by the Coulomb barrier height V_B, continuum-continuum couplings are excluded from the couplings matrix elements "No ccc".

and fusion cross sections, plotted in figure.5.8, is the ratio σ_x/σ_x^{ncc}, where σ_x ($x \equiv$ BU, TF) is the breakup/total fusion cross section obtained with the inclusion of all the various couplings in the coupling matrix elements and σ_x^{ncc}, the breakup/total fusion cross section obtained when the continuum-continuum couplings are removed. Observing that Figure 5.8, one sees that for $E_{cm}/V_{\rm B} < 1$, $\sigma_{\rm TF}/\sigma_{\rm TF}^{ncc} < \sigma_{\rm BU}/\sigma_{\rm BU}^{ncc}$, whereas for $E_{cm}/V_{\rm B} > 0.9$, $\sigma_{\rm TF}/\sigma_{\rm TF}^{ncc} > \sigma_{\rm BU}/\sigma_{\rm BU}^{ncc}$. In other words, the breakup cross section is more enhanced by the continuum-continuum couplings at sub-barrier energies compared to the fusion cross section. For energies above the barrier, the breakup cross section more suppressed by these couplings. We shall emphasize that in the calculation of the fusion cross section, we did not use short-range nuclear potentials as it is usually done when one is only interested in fusion cross section, as one can see for example in Ref. [68]. Also, the longer tail of the projectile ground-state wave function means that the diagonal nuclear potential given by equation (4.11), has a longer tail and can account for nuclear absorption outside the absorption region. The will result in the increase of the total fusion cross section, as pointed out in Ref. [68]. However, this is not expected to have any meaningful effect on the results reported in the figures above. What can we learn from the enhancement of the breakup cross section at sub-barrier energies? Notice that couplings to continuum states result in the delay of the breakup process. This is due to the multi-step process nature of such couplings as opposed to single step couplings to and from the ground state. For energies above the Coulomb barrier, delaying the breakup implies the increase of the probability of the breakup occurring within the interaction region where nuclear forces are active to trigger absorption. That can explains the importance of the total fusion cross section over the breakup cross section at above the Coulomb barrier incident energies in figure 5.4. In the same energy region, with the exclusion of the continuum-continuum couplings, the breakup becomes more prompt, meaning that after breakup the projectile fragments have enough time to survive absorption. This assertion can justify the importance of the breakup cross section over the total fusion cross section in figure 5.5. Considering incident energies below the Coulomb barrier, the projectile is slower due to its low incident energy, and it is further slows down by the Coulomb repulsion, since on its incoming trajectory, the projectile's motion is opposed to the projectile-target Coulomb force. The loss in the projectile kinetic energy can be exacerbated by including the

continuum-continuum couplings, since energy will be required to excite these states. As such, not enough projectile kinetic energy might be left to trigger the projectile breakup on its incoming trajectory. This implies that the projectile could be excited to its continuum states without breaking up. However, on the outgoing trajectory, the projectile gains an initial kinetic energy as its leaves the target because in this case it is accelerated by the projectile-target Coulomb force. On both incoming and outgoing projectile projectile trajectories, the continuum-continuum couplings play the same role, which is to delay the breakup process. The delay caused by these couplings together with the projectile acceleration coming from the projectile-target Coulomb force, ensure that the projectile breaks up on its outgoing trajectory away from the absorption region out of the reach of nuclear forces. This will reduce the fusion cross section but will increase the breakup cross section as less amount of flux is removed from the breakup channel to feed up the fusion channel. Therefore, the enhancement of the breakup cross section at sub-barrier by the continuum-continuum couplings can be explained by the breakup on the projectile outgoing trajectory. The breakup on the projectile outgoing trajectory at sub-barrier incident energy is discussed in Refs. [95, 96]. The argument that on the outgoing trajectory the projectile could breakup away from the reach of the nuclear forces can be substantiated by showing that at sub-barrier energies, the enhancement of the breakup cross section is due to its Coulomb breakup component. This inference is born out of the fact that in that case, the nuclear breakup will increasingly become irrelevant as the projectile progresses away from the target nucleus. One can then expect the Coulomb breakup cross section to be enhanced by the continuum-continuum couplings. To show this, in the next section we analyse the Coulomb as well as nuclear breakup cross sections.

5.4 Coulomb and nuclear breakup cross sections

In order to further test that the enhancement of the breakup cross section by the continuum-continuum couplings at deep sub-barrier energies could hint at a projectile breakup on its outgoing trajectory, we propose to analyses the Coulomb as well as nuclear breakup cross sections. Notice that the breakup of the projectile nucleus comes from its interaction with the target nucleus via Coulomb and nuclear forces. The Coulomb interaction produces

the Coulomb breakup, whereas the nuclear interaction produces the nuclear breakup. Because of the long-range character of Coulomb forces and the short-range nature of nuclear forces, the former are responsible for an asymptotic breakup (away from the target), whereas the breakup caused by nuclear forces occurs when the projectile reaches the neighbourhood of the target nucleus. Due to the asymptotic component of the Coulomb breakup, lower projectile continuum partial wave such as p-wave are known to contribute the largest portion of the Coulomb breakup cross section, and this is in fact the essence of the first-order approximation theory. Coulomb and nuclear breakups are regarded as components of the total breakup cross section, and this is the breakup cross section that we have so far discussed in the previous sections. It is obtained when both Coulomb and nuclear interactions are simultaneously included in the coupling matrix elements. Such breakup cross section contains the effect of the Coulomb-nuclear interference which we will discuss later. To Separate the total breakup cross section into Coulomb and nuclear components remains a major challenge for breakup reaction theories. In this work we do not intend to perform such task, but we rather resort to the following approximate procedure to obtain the Coulomb and nuclear breakup cross sections. To calculate the Coulomb breakup cross section, we removed all the core-target and neutron-target nuclear interactions from the coupling matrix elements (3.25), keeping only its monopole component in the elastic scattering channel [it is given by equation (3.6), where the core-target coordinate R_{cvt}, is replaced by the projectile-target center-of-mass coordinate R]. To this potential we added the monopole nuclear potential given by equation (4.11), with both its real and imaginary parts. In that case, the Coulomb breakup cross section is affected by the absorption in the elastic scattering channel because of to the imaginary part of this potential. Similarly, the nuclear breakup cross section was calculated by removing the core-target Coulomb potential from the coupling matrix elements, also keeping the projectile-target Coulomb and nuclear monopole potentials in the elastic scattering channel. This procedure, although approximate, has been shown to yield the desired effect. The Coulomb and nuclear breakup cross sections thus obtained are shown in figure 5.9, where results are shown with the inclusion and exclusion from the coupling matrix elements of the continuum-continuum couplings. Indeed, in that figure, we notice that at sub-barrier energies, the Coulomb breakup cross section is strongly enhanced by the
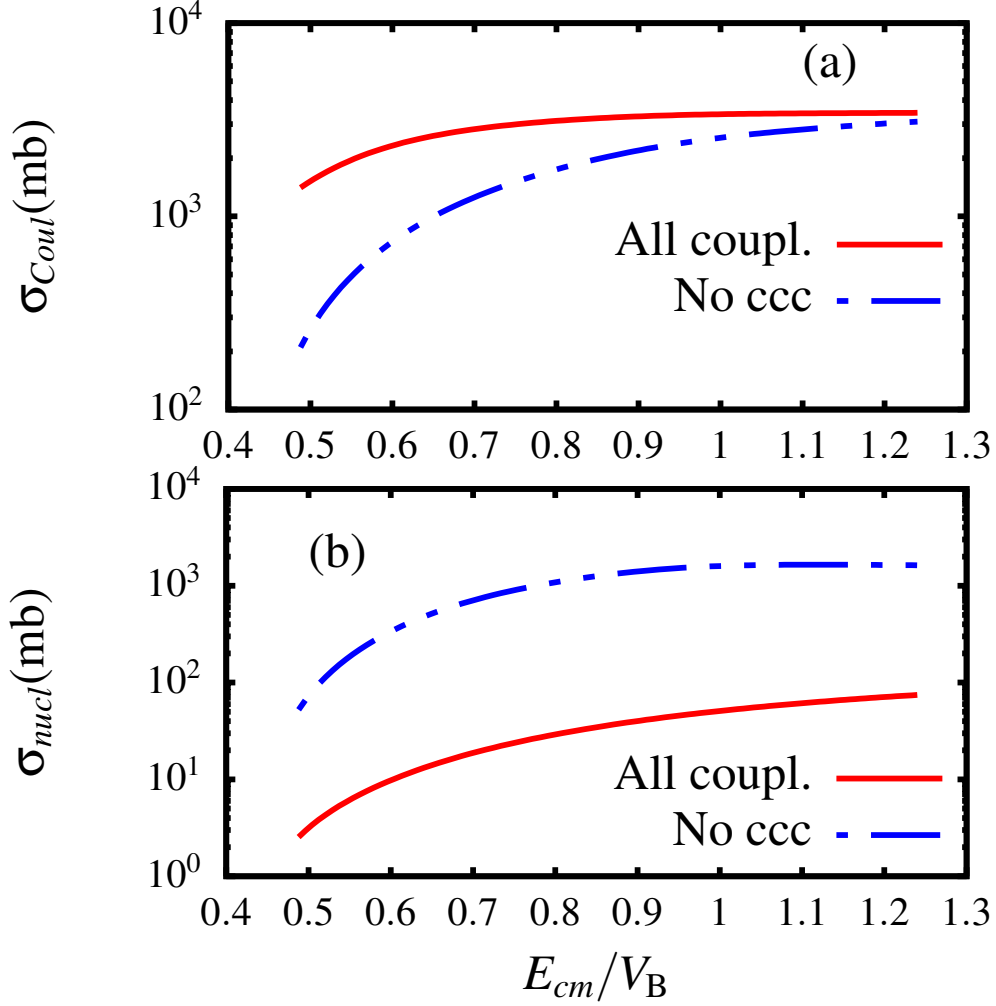
Figure 5.9: Coulomb breakup cross sections [panel (a)] and nuclear breakup cross sections [panel (b)] plotted as functions of the incident energy scaled by the Coulomb barrier height V_B, and obtained when the continuum-continuum couplings are included and excluded from the coupling matrix elements.

continuum-continuum couplings [see panel (a)]. Therefore, the results in this figure concurs with our assessment in Section 5.3.1, that if the breakup occurs on the outgoing trajectory, the continuum continuum couplings are expected to enhance the Coulomb breakup cross section. One may further argue that enhance of the breakup cross section by these couplings could be characteristic of a projectile breakup on the outgoing trajectory. One further sees that as the incident energy increases, the enhancement strength decreases and the trend suggests that at higher incident energies, continuum-continuum couplings would amount to a smaller effect on the Coulomb breakup cross section. In fact, it has been shown that at higher incident energy, these couplings have limited suppression effect on the Coulomb breakup cross section (for example, see Ref. [4]). Contrary
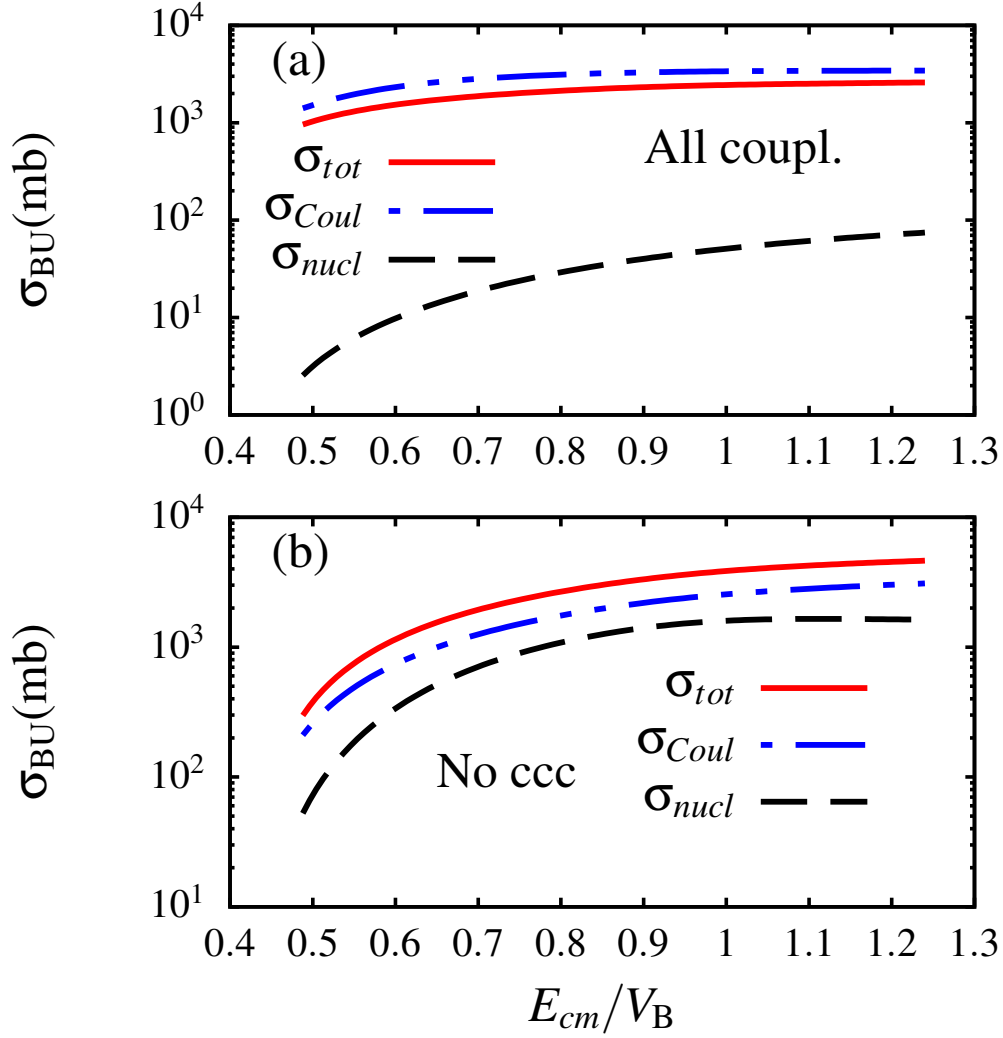
Figure 5.10: Total, nuclear and Coulomb breakup cross sections shown as functions of the incident energy scaled by the Coulomb barrier height V_B, obtained in the case where the continuum-continuum couplings are included in [panel (a)] and removed from the coupling matrix elements in [panel (b)] .

to the Coulomb breakup, panel (b) of that figure, shows that the nuclear breakup cross section is largely suppressed by continuum-continuum couplings at all the displayed incident energy region. At energies above the barrier, the nuclear breakup cross section has been reported to be strongly suppressed by these couplings compared to the Coulomb breakup cross section. Actually, as shown in Ref. [4], this suppression is reported as one of the main reasons why the Coulomb breakup is substantially dominant over the nuclear breakup in reactions involving heavy targets. It then inferred in that reference, that a larger target charge alone cannot justify the importance of the Coulomb breakup over the nuclear breakup in the breakup of loosely-bound systems. To better display this aspect,

Table 5.1: Integrated total, nuclear and Coulomb breakup cross sections (millibarns) with the inclusion of all the various couplings (σ_{tot}, σ_{Coul}, σ_{nucl}) and when the ccc are excluded (σ_{tot}^{ncc}, σ_{Coul}^{ncc}, σ_{nucl}^{ncc}), $\kappa = 1 - \sigma_{tot}/(\sigma_{Coul} + \sigma_{nucl})$ and $\kappa^{ncc} = 1 - \sigma_{tot}^{ncc}/(\sigma_{Coul}^{ncc} + \sigma_{nucl}^{ncc})$ is the measure of the Coulomb-nuclear interference.

E_{cm}/V_B	All couplings				No cc couplings			
	σ_{coul}	σ_{nucl}	σ_{tot}	κ	σ_{coul}^{ncc}	σ_{nucl}^{ncc}	σ_{tot}^{ncc}	κ^{ncc}
0.488	1407	2.540	960	0.3189	210	52	298	-0.1374
0.550	1994	5.615	1352	0.3239	465	150	708	-0.1512
0.614	2546	9.970	1644	0.3568	790	332	1248	-0.1123
0.677	2920	15.33	1872	0.3623	1144	587	1808	-0.0445
0.739	3128	21.59	2065	0.3444	1494	876	2319	0.0215
0.864	3303	36.01	2312	0.3076	2108	1402	3183	0.0932
0.956	3376	46.65	2423	0.2921	2458	1617	3721	0.0869
1.005	3396	51.65	2462	0.2859	2599	1653	3938	0.0738
1.145	3414	65.83	2545	0.2686	2921	1651	4393	0.0392
1.240	3435	74.47	2593	0.2611	3093	1628	4632	0.0189

in figure 5.10, we plot on the same panels, the total, Coulomb and nuclear breakup cross sections. In panel (a) of that figure, we have shown the results obtained with the inclusion of all the different couplings and the results obtained with the exclusion of the continuum-continuum couplings in panel (b). In panel (a), one sees that the nuclear breakup cross section is just a fraction of the Coulomb and total breakup cross section. This was expected given the fact that the reaction at hand is considered to be a Coulomb-dominated reaction, given the large electric charge of the target. However, in panel (b), we notice a competition between the Coulomb and nuclear breakup cross sections. For a further assessment of continuum-continuum couplings effect on the total, Coulomb and nuclear breakup cross sections, Table 5.1 summarizes the integrated total, Coulomb and nuclear breakup cross sections obtained when the continuum-continuum couplings are included and excluded from the coupling matrix elements. Contemplating that table, one observes (as we have already seen in figure 5.9), a huge enhancement of the Coulomb breakup cross section due to the continuum-continuum couplings. For instance at $E_{cm}/V_B = 0.488$, we deduce that the Coulomb breakup cross section is enhanced by factor of about 7.0, the total breakup cross section by a factor of about 3.0, whereas the nuclear breakup cross

section is suppressed by a fact of about 20.0. at $E_{cm}/V_B = 1.24$, we deduce that the Coulomb breakup cross section enhanced by factor of about 1.0, the total breakup cross section is suppressed by a factor of about 2.0, whereas the nuclear breakup cross section is suppressed by a fact of about 22.0. The enhancement or suppression factor was obtained from the ratio of the larger breakup cross section to the small breakup cross section. It follows that the nuclear breakup cross section is more affected by the continuum-continuum couplings compared to the Coulomb breakup cross section. Among other factors, this is mainly due to the fact that the nuclear breakup occurs in the vicinity of the target nucleus where couplings to higher partial waves are important. A further comparison between the Coulomb and nuclear breakup cross section, when the continuum-continuum couplings are included, one sees that for all the incident energy considered, the Coulomb breakup cross section is larger than the total breakup cross section, whereas the nuclear breakup cross section is just a fraction of the Coulomb and total breakup cross section. For instance, at $E_{cm}/V_B = 0.488$, the nuclear breakup cross section represents about 0.20% and 0.3% of the Coulomb and total breakup cross sections, respectively. For $E_{cm}/V_B = 1.2$, the nuclear breakup cross section represents about 2.0% and 3.0% of the Coulomb and total breakup cross sections, respectively. However, when the continuum-continuum couplings are removed, the nuclear breakup cross section rapidly grows such that for example, at $E_{cm}/V_B = 0.488$, now the nuclear breakup cross section represents about 25.0% and 17.0% of the Coulomb and total breakup cross sections, respectively. For $E_{cm}/V_B = 1.2$, the nuclear breakup cross section represents about 52.0% and 35.0% of the Coulomb and total breakup cross sections, respectively. These numbers indicate that the dominance of the Coulomb breakup cross section over its nuclear counterpart is not only related to the larger electric charge of the target nucleus but also to stronger continuum-continuum couplings in the nuclear breakup case.

5.4.1   Coulomb-nuclear interference

It is known that when Coulomb and nuclear forces are simultaneously included into the coupling matrix elements, they interfere to create the total breakup. This interference has been found to be quite significant even when the nuclear breakup is itself regarded as negligible. To estimate this interference, we compare the breakup cross section obtained

when the Coulomb and nuclear forces are simultaneously included into the coupling matrix elements (i.e., coherent sum of the Coulomb and nuclear breakup cross sections), and the breakup cross section obtained by summing up the Coulomb and nuclear breakup cross sections (i.e., incoherent sum of the Coulomb and nuclear breakup cross sections). Notice that in the calculations of the individual Coulomb and nuclear breakup cross sections, the Coulomb-nuclear interference is not taken into account except in the diagonal channel. This because in both calculations, the projectile-target Coulomb and nuclear monopole potentials in the elastic scattering channel are included as outlined in Section 5.4. We estimate the strength of the Coulomb-nuclear interference as follows:

$$\kappa = 1 - \frac{\sigma_{tot}}{\sigma_{Coul} + \sigma_{nucl}}, \tag{5.1}$$

where $\sigma_{Coul} + \sigma_{nucl}$, the incoherent sum of both Coulomb and nuclear breakup cross sections. The values of κ are given in columns 5 (when continuum-continuum couplings are included) and 9 (when continuum-continuum couplings are excluded). According to equation (5.1), if $\kappa \to 0$, then $\sigma_{tot} \to \sigma_{Coul} + \sigma_{nucl}$. In this case there is no Coulomb-nuclear interference or rather that this interference is very weak. If $\kappa > 0$, then $\sigma_{tot} < \sigma_{Coul} + \sigma_{nucl}$. In this case, the interference is destructive as it lowers the total breakup cross section. If $\kappa < 0$, then $\sigma_{tot} > \sigma_{Coul} + \sigma_{nucl}$. In this case, the interference is constructive as it increases the total breakup cross section. Now examining Table 5.1, it follows that this interference is exclusively destructive when all the couplings are included. When the continuum-continuum couplings are removed, this interference is constructive for $E_{cm}/V_{\mathrm{B}} \leq 0.677$, and becomes weakly destructive at larger incident energies.

Chapter 6

Concluding Remarks

In this dissertation we have investigated the breakup of the ^{11}Be weakly-bound neutron-halo nucleus on a lead target, considering an incident energy range below and around the Coulomb barrier. We first provided a detailed quantum mechanical description of bound and scattering states of the two-body projectile nucleus, where a valence neutron is loosely-bound to the core nucleus. Then, a three-body quantum system was obtained through the interaction of the projectile with the target nucleus. For the sake of simplicity, and in order to reduce the computational burden, explicit target excitations were not taken into account, except those induced by the projectile-target optical interactions. In order to handle such a complex system, we employed to the continuum discretized coupled channels (CDCC) formalism, where the three-body scattering wave function is expanded on a basis formed by the internal projectile states, namely the bound and scattering states. However, given the infinite number of scattering states together with the oscillatory behaviour of the scattering wave functions, we employed the binning technique of the CDCC formalism, and truncated the linear scattering momentum k by k_{max} and discretized the truncated momentum space into momentum bins. With this procedure, the pure scattering wave functions were transformed into square-integrable bin wave functions, leading to a finite and orthogonal expansion basis. Expanding the wave function on that basis and its substitution in the Schrödinger equation of the three-body system, yielded a finite set of coupled differential equations. The derivation of the analytical expression of the resulting coupling matrix elements is also provided. The set of coupled differential equations was numerically solved, with the appropriate asymptotic boundary conditions to obtain the scattering matrix elements. The latter were then used to construct the breakup observables. To test the stability of the numerical calculations, the convergence of the angular-distributions differential breakup cross sections was tested against various

numerical parameters, such as maximum value of the core-neutron orbital angular momentum ℓ_{max}, the maximum value of the core-neutron internal radial coordinate, r_{max}, the maximum value of the core-neutron excitation energy, ε_{max}, and the maximum multipole order expansion λ_{max}. Although the convergence was tested for all the incident energies considered, only the results obtained for $E_{cm}/V_{\mathrm{B}} = 0.9$, $E_{cm}/V_{\mathrm{B}} = 1.0$ and $E_{cm}/V_{\mathrm{B}} = 1.2$ incident energies, where $V_{\mathrm{B}} = 38.87\,\mathrm{MeV}$, were displayed. It is found that a much larger breakup space is not needed to obtained converged breakup cross sections. A satisfactory convergence was obtained for $(\ell_{max}, \varepsilon_{max}, \lambda_{max}, r_{max}) = (3\hbar, 6\,\mathrm{MeV}, 3, 60\,\mathrm{fm})$.

The stability of the numerical calculations was further tested by comparing the numerical results with the experimental data. Owing to the lack of experimental data in the energy range of interest in the present dissertation, numerical calculations were performed considering an incident energy of $E_{lab} = 140\,\mathrm{MeV}$, at which the $^{11}\mathrm{Be} + {}^{208}\mathrm{Pb}$ reaction has been measured. A satisfactory description of the experimental data is obtained even though the inelastic breakup component was not included in the numerical calculations, unlike in some other studies. To investigate whether the breakup channel could be the dominant reaction channel at deep sub-barrier energies for the reaction at hand, we compared the breakup cross section with the total fusion cross section. Indeed, it is found that the breakup cross section is more important than the total fusion cross section for incident energies below the Coulomb barrier, whereas above the Coulomb barrier, the total fusion cross section more important. The similarity of these results with the results obtained with other loosely-bound projectiles such as $^{8}\mathrm{B}$ and $^{6}\mathrm{Li}$, could signal the universality of this feature in breakup reactions induced by weakly-bound systems at low incident energy regime. In order to probe the origin of this importance, we performed a series of calculations where the continuum-continuum couplings were removed from the coupling matrix elements. In that case, only couplings to and from the bound state were taken into account. It is found that below the Coulomb barrier, the breakup and total fusion cross sections become almost similar, with their respective curves hardly distinguishable. For incident energy above the Coulomb barrier, the breakup cross section becomes slightly larger. Therefore, we concluded that the importance of the breakup cross section over the total fusion cross section is actually due to the effect of the continuum-continuum couplings. To better understand this effect, we separately analysed the role of these couplings

on both cross sections. It is found that below the Coulomb barrier, these couplings serve to enhance the breakup and total fusion cross sections, whereas they are both suppressed above the Coulomb barrier. A further analysis showed that the breakup cross section is strongly enhanced compared the total fusion cross section, and also it is more suppressed above the Coulomb barrier.

To further probe the enhancement of the breakup cross section by the continuum-continuum couplings, we analysed the Coulomb and nuclear breakup cross sections, which are components of the total breakup cross section that is discussed above. The process to calculate the Coulomb and nuclear breakup cross sections was first outlined. It is shown that below the Coulomb barrier, the Coulomb breakup cross section is strongly enhanced by the continuum-continuum couplings, whereas the nuclear breakup cross section is strongly suppressed. It followed that the enhancement of the total breakup cross section by these couplings comes exclusively from its Coulomb component. It is argued that the enhancement of the Coulomb breakup cross section below the Coulomb barrier by the continuum-continuum couplings can be explained by the projectile breakup on its outgoing trajectory.

In conclusion, a dominant breakup channel over other reaction channels at deep sub-barrier energies could be a universal feature in the breakup of weakly-bound systems and may be justified by the projectile breakup on its outgoing trajectory. It could be interesting to extend this study four-body breakup reactions, where the projectile is a three-body weakly-bound system such as ^{6}He, ^{19}B, ^{22}C, among others.

Bibliography

[1] I. Tanihata, H. Hamagaki, O. Hashimoto *et al.*, *Phys. Rev. Lett.* **55**, 2676 (1985).

[2] I. Tanihata, H. Savajols and R. Kanungo, *Prog. Part. Nucl. Phys.* **68**, 215-313 (2013)

[3] Bahati Mukeru, Tobias Frederico and Lauro Tomio, *Phys. Rev.* **C 102**, 064623 (2020).

[4] Bahati Mukeru and Lauro Tomio, *Chin. Phys.* **C 46**, 014103 (2022).

[5] Bahati Mukeru *J. Phys. G: Nucl. Part. Phys.* **45**, 065201 (2018).

[6] J. A. Tostevin, F. M. Nunes and I. J. Thompson *Phys.Rev.* **C 63**, 024617 (2001).

[7] F. F. Duan, Y. Y. Yang, J. Lei *et al.*, *Phys.Rev.* **C 105**, 034602 (2022).

[8] Pierre Capel, D. R. Phillips, H. W. Hammer, *Phys. Lett.* **B 825**, 136847 (2022).

[9] Bahati Mukeru, Jesus Lubian and Lauro Tomio, *Phys. Rev.* **C 105**, 024603 (2022).

[10] Bahati Mukeru, Lucas V. Ndala and Mantile L. Lekala, *Nucl. Phys.* **A 1020** 122397 (2022).

[11] Bahati Mukeru, *Chin. Phys.* **C 45**, 054107 (2021).

[12] Bahati Mukeru, *Int. J. Mod. Phys.* E **30**, 2150006 (2021).

[13] T. Aumann, C. Barbieri, D. Bazin *et al.*, *prog. Part. and Nucl. Phys.* **118**, 103847 (2021).

[14] L. R. Gasques, M. A. G. Alvarez, A. Arazi *et al.*, *Phys. Rev.* **C 103**, 034616 (2021).

[15] Pierre Capel, R. C. Johnson, and F. M. Nunes, *Eur. Phys. J.* **56**, 300 (2020).

[16] N. Fukuda, T. Nakamura, N. Aoi *et al.*, *Phys. Rev.* **C 70**, 054606 (2004).

[17] M. Wang, G. Audi, F. G. Kondev, *et al.*, *Chin. Phys.* **C 41**, 3, 030003 (2017).

[18] D. S. Ahn, N. Fukuda, H. Geissel *et al.*, *Phys. Rev. Lett.* **123**, 212501 (2019).

[19] H. L. Crawford, P. Fallon, A. O. Macchiavelli *et al.*, *Phys. Rev. Lett.* **122**, 052501 (2019).

[20] N. Kobayashi, T. Nakamura, Y. Kondo *et al.*, *Phys. Rev. Lett.* **112**, 242501 (2014).

[21] A. Pakou, L. Acosta, P. D. O'Malley *et al.*, *Phys. Rev.* **C 102**, 031601(R) (2020).

[22] Bahati Mukeru, Lucas V. Ndala and Mantile L. Lekala, *Pramana. J. Phys.* **95** 106 (2021).

[23] Bahati Mukeru, Mantile L. Lekala , Andrey S. Denikin, *Nucl.Phys.* **A 935**, 18-27 (2015).

[24] Bahati Mukeru, Mantile L. Lekala and Andrey S. Denikin *J. Phys. G: Nucl. Part.* **42**, 015109 (11pp) (2015).

[25] Luiz F. Canto, Jesus Lubian, Paulo R. S. Gomes *et al.*, *Phys.Rev.* **C 80**, 047601 (2009).

[26] A. Diaz-Torres and Ian J. Thompson, *Phys.Rev.* **C 65**, 024606 (2002).

[27] Filomena M. Nunes and Ian J Thompson, *Phys. Rev.* **59**, 2652-2659 (1999).

[28] T. Motobayashi, N. Iwasa, Y. Ando *et al.*, *Phys. Rev.Lett.* **73**, 2680 (1994).

[29] T. Kido, K. Yabana and Y. Suzuki, *Phys. Rev.* **C 53**, 2296 (1996).

[30] A. Diaz-Torres, *Phys.Rev.* **C 68**, 044607 (2003).

[31] E. F. Aguilera, E. Martinez-Quiroz, D. Lizcano *et al.*, *Phys.Rev.* **C 79**, 021601 (2009).

[32] L. Yang, C. J. Lin, H. Yamaguchi *et al.*, *Phys. Lett.* **B 813**, 136045 (2021).

[33] A. Ozawa, T. Suzuki, I. Tanihata, *Nucl.Phys.* **A 693**, 32-62 (2001).

[34] S. Ogawa and T. Matsumoto, *Phys. Rev.* **C 105**, L041601 (2022).

[35] H. Kumawat, Vivik V. Parkar, T. N. Nag *et al.*, *Phys. Rev.* **C 105**, 024611 (2022).

[36] D. Valiolda, D. Janseitov , V. Melezhik, *Eur. Phys. J.* **A 58**, 34 (2022).

[37] M. Dan , R. Chatterjee, M. Kimura, *Eur. Phys. J.* **A 57**, 203 (2021).

[38] L. A. Souza, E. V. Chimanski, and B. V. Carlson *Braz. Phys.J.* **A 51**, 323(2021).

[39] Angela Bonaccorso, D. M. Brink, *Eur. Phys. J.* **A 57**, 171 (2021).

[40] Bahati Mukeru, *Phys. Comm. J* **5** ,075004 (2021).

[41] Valdir Guimaráes, E. N. Cardozo, Jesus Lubian *et al.*, *Eur. Phys. J. A.* **57** 90 (2021).

[42] O. C. B. Santos, R. Lichtenthäler , K. C. C. Pires *et al.*, *Phys. Rev.* **C 103**, 064601 (2021).

[43] Luis F. Canto, Valdir Guimarães, J. Lubian *et al.*, *Eur. Phys. J.* **56**, 281 (2020).

[44] Vishwajeet Jha, Vivik V. Parkar, and S. Kailas, *Phys. Rep.* **845**, 1 (2020).

[45] K. J. Cook, T. Nakamura, Y. Kondo *et al.*, *Phys. Rev. Lett.* **124**, 212503 (2020).

[46] Y. S. Neoh, M. Lyu, Y. Chazono *et al.*, *Phys. Rev.* **C 101**, 054606 (2020).

[47] Bahati Mukeru, Mantile L. Lekala, J. Lubian *et al.*, *Nucl. Phys.* **A 996** 121700 (2020).

[48] T. Otsuka, A. Gade, O. Sorlin *et al.*, *Rev. Mod. Phys.* **92** 015002 (2020).

[49] X. N. Cao, Q. Liu and J. Y. Guo, *Phys. Rev.* **C 99** 014309 (2019).

[50] R. Chatterjee and R. Shyam, *Nucl.Phys.* **103**, 67 (2018).

[51] V. Soukeras, A. Pakou, F. Cappuzzello *et al.*, *Phys.Rev.* **C 95**, 054614 (2017).

[52] Luiz F Canto, Paulo R. S Gomes, R. Donangelo *et al.,, Phys.Rep.***596**, 1 (2015).

[53] J. J. Kolata, V. Guimarães and E. F. Aguilera *Eur. Phys. J. A* **52**, 123 (2016).

[54] D. R. Otomar, P. R. S. Gomes, Jesus Lubian *Phys.Rev.* **C 87**, 014615 (2013).

[55] Luiz F. Canto, and Mahir S. Hussein,World. scientific. **chap. 2, p. 51**, Singapore (2013).

[56] Tobias Frederico, A. Delfino, Lauro Tomio *et al.*, *Progr.Part.Nucl.Phys.* **67**, 939-994 (2012).

[57] R. Linares, M. Sinha, E. N. Cardozo et al., *Phys.Rev.* **C 103**, 044613 (2021).

[58] Pierre Descouvemont and Daniel Baye, *Rep. Prog. Phys.* **73**, (2010).

[59] A. Di Pietro, G. Randisi, V. Scuderi *et al.*, *Phys. Rev. Lett.* **105**, 022701 (2010).

[60] H. Esbensen, *Phys.Rev.* **C 80**, 024608 (2009).

[61] N. C. Summers, F. M. Nunes, and I. J. Thompson *Nucl.Phys.* **C 74**, 014606 (2006).

[62] A. S. Jensen, K. Riisager, D. V. Fedorov *et al.*, *Rev. Mod. Phys.* **76**, 215 (2004).

[63] T. Egami, K. Ogata, T. Matsumoto *et al.*, *Phys.Rev.* **C 70**, 047604 (2004).

[64] Pierre Capel, Daniel Baye, and V. S. Melezhik *Phys.Rev.* **C 68**, 014612 (2003).

[65] Carlos A. Bertulani, P. Danielewicz *Nucl.Phys.* **A 717**, 199-213 (2003).

[66] T. Matsumoto, T. Kamizato, K. Ogata Lukyanov *Phys.Rev.* **C 68**, 064607 (2003).

[67] Y. Hirabayashi and Y. Sakuragi *Phys. Lett.* **69**, 1892 (1992).

[68] M. R. Cortes, J. Rangel, J. L. Ferreira, and J. Lubian *Phys. Rev.* **C 102** , 064628 (2020).

[69] A. V. Karpov, Andrey S. Denikin, M. A. Naumenko *et al.*, *Phys. Res.* **A 859** 112-124 (2017).

[70] M. S. Golovkov, L. V. Grigorenko, A. S. Fomichev, *et al.*, *Phys. Rev.* **C 72.** 064612 (2005).

[71] S. M Lukyanov, Andrey S. Denikin, E. I. Voskoboynik ,*et al.*, *J. Phys. G: Nucl. Part. Phys.***3** , 035102 (2014).

[72] E. Y. Nikolskii, A. A Korsheninnikov, H. Otsu, *et al. Phys. Rev. C. Nucl. Phys.* **81**,6, 064606 (2010).

[73] Andrey S. Denikin, S. M. Lukyanov, N. K. Skobelev, *et al.*, *Phys. Part. Nucl. Lett* **12**, 5, 703-712 (2015).

[74] B. A. Urazbekov, N. Itaco, Andrey S. Denikin, *et al.*, *J. Phys. G: Nucl. Part. Phys.* **46.** 10, 105110 (2019).

[75] Andrey S. Denikin, V. I. Zagrebaev, Pierre Descouvemont *Phys. Rev. C: Nucl. Phys.* **79.** 2, 024605 (2009).

[76] N. A. Elmahdy, A. S. Denikin, M. Ismail, *et al.*, *Eur. Phys. J. A* **51**,5, 62 (2015).

[77] C. Fougéres, F. de Oliveira Santos, J. José, *et al. Nat. Comm* **14**, 4536. (2023).

[78] J. C. Zamora , J. L. Ferreira, A. Barioni,*et al.*, *Phys. Rev.* **C 106**, 014603 (2022).

[79] K. Wang, Y. Y. Yang, V. Guimaraes, *et al.*, *Phys. Rev.* **C 105**, 054616 (2022).

[80] G. Kaur, Valdir Guimarães, J. C. Zamora, *et al.*, *Phys. Rev.* **C 105**, 024609 (2022).

[81] C. Zamora, Valdir Guimaraes, G. V. Rogachev, *et al.*, *Phys. lett.* **B 816**, 136256 (2021).

[82] Y. Kuçuk, Valdir Guimaraes, B. V. Carlson. *Eur. Phys. J. A* **57**,87, (2021).

[83] Luis F. Canto, Valdir Guimarães, Jesus Lubian *et al.*, *Eur. Phys. J. A* **56** (2020).

[84] Valdir Guimarães, E. N. Cardozo, V. B. Scarduelli, *et al.*, *Phys. Rev.* **C 100**, 034603(2019).

[85] Valdir Guimarães, Jesus Lubian, J. J. Kolata, *et al.*, *Eur. Phys. J. A* **54** (2018).

[86] Valdir Guimarães, J. J. Kolata, E. F. Aguilera,*et al.*, *Phys. Rev.* **C 93**, 064607 (2016).

[87] A. Barioni, Valdir Guimarães, A. Lepine-Szily, *et al.*, *Phys. Rev.* **C 80**, 034617 (2009).

[88] Valdir Guimarães, O. Camargo, R. Lichtenthaler, *et al.*, *Phys. Rev.* **C 75**, 054602-1(2009).

[89] I. Tanihata, *J. Phys. G: Nucl. Part. Phys.* **22**, 157 (1996).

[90] P. G. Hansen, A. S. Jensen and B. Jonson, *Annu.Rev. Nucl. Part. Sci.* **45**, 591-634 (1995).

[91] Y. Iseri, M. Yahiro and M. Kamimura *Prog. Theory. Phys. Suppl.* **89**, 84-117 (1986).

[92] N. Austern, Y. Iseri, M. Kamimura *et al.*, *Phys. Rep* **154**, 125-204 (1987).

[93] R. Y. Rasoanaivo, and George H. Rawitscher, *Phys. Rev.* **C 39**, 1709 (1989).

[94] Bahati Mukeru, *EPL* **143**, 64003 (2023).

[95] L. Yang, C. J. Lin, H. Yamaguchi *et al.*, *Nat. Comm* **13**:7193(2022).

[96] H. Zhang, *Science Bulletin* **68** 2-4 (2023).

[97] Bahati Mukeru and Mantile L Lekala, *Phys. Rev.* **C 91**, 064609 (2015).

[98] R. Spartà, A. Di Pietro, P. Figuera *et al.*, *Phys. Lett.* **B 820**, 136477 (2021).

[99] N. C. Summers, F. M Nunes, *Phys. Rev.C* (2004).

[100] M. Abramowitz and I. A. Stegun *Handbook of Mathematical Functions with Formulas* Vol.55, (1972).

[101] A. R. Edmond *Angular momentum in quantum mechanics*, Princeton University press, Princeton (1957).

[102] G. D. Kolinger, Luis F. Canto, R. Donangelo *et al.*, *Phys. Rev.* **C 98** 044604,(2018).

[103] S. Hashimoto, K. Ogata, S. Chiba, M. Yahiro, *Prog. Theory. Phys.* 122, 1291 (2009).

[104] Pierre Descouvemont, Luis F. Canto, and Mahir S. Hussein *Phys. Rev.* **C** (2017).

[105] T. Nakamura, S. Shimoura, T. Kobayashi *et al.*, *Phys, Lett,* **B 331**, 296-301(1994).

[106] C. J. Lin, H. Q Zhang, Z. H Liu *et al.*, *Phys.Rev.* **C 66**, 067302 (2002).

[107] F. F. Duan, Y. Y. Yang, K. Wang *et al.*, *Phys.Rev.lett* **B 811**, 135942 (2020).

[108] Pierre Capel, G. Goldstein and Daniel Baye *Phys.Rev.* **C 70**, 064605 (2004).

[109] https://www.nndc.bnl.gov/nudat3.

[110] N. Fukuda, T. Nakamura, T. Kobayashi *et al.*, *Prog. Theo. phys.* **146**, 462(2002).

[111] A. J. Koning and J. P. Delaroche, *Nucl. Phys.* **A 713**, 231 (2003).

[112] Bahati Mukeru and Mukeru L. Lekala *Phys.Rev.***C 94**, 024602(2016).

[113] Bahati Mukeru, G. J Rampho and Mantile L Lekala *J. Phys.G: Nucl.Part. Phys.***45**, 045101(2018).

[114] Ian J. Thompson and Filomena M. Nunes, *Cambridge University Press,New York,*(2009).

[115] Ian J. Thompson *Comp.Phys.* **Rep 7**, 167-212 (1988).

[116] R. O. Akyuz and A. Winther *Proc. Enrico. Fer. Int. Phys.* (1979).

[117] Carlos A. Bertulani and G. Baur *Phys* **Rep 163**, 299 (1988).

[118] K. Alder, A. Bohr, T Haus *et al.*, *Rev. Mod. Phys*, **28**, 432(1956).

[119] G. Baur and H. Rebel *Annu. Rev. Nucl.Part.Sci.***46**, 321(1996).

[120] G. Baur, K. Hencken and D. Trautmann *Prog.Part. Nucl.Phys.***51**, 487(2003).

[121] L. C. Chamon, B. V. Carlson, L. R. Gasques *et al.*, *Phys. Rev.* **C 66**, 014610(2002).

[122] P. G. Hansen and B. M. Sherrill, *Nucl. Phys.* **A 693** 133 168 (2001).

[123] Carlos A. Bertulani, *Comp. Phys. Comm.* **156**, 123(2003).